

PKS 2131–021 – Discovery of Strong Coherent Sinusoidal Variations from Radio to Optical Frequencies: Compelling Evidence for a Blazar Supermassive Black Hole Binary

S. KIEHLMANN,¹ P. V. DE LA PARRA,² A. G. SULLIVAN,³ A. SYNANI,^{4,1} I. LIODAKIS,^{1,5} A. C. S. READHEAD,^{1,6} M. J. GRAHAM,⁷ M. C. BEGELMAN,^{8,9} R. D. BLANDFORD,^{3,10,11} K. CHATZHOANNOU,^{12,13} Y. DING,¹⁴ F. HARRISON,¹⁴ D. C. HOMAN,¹⁵ T. HOVATTA,^{16,17} S.R. KULKARNI,¹⁴ M.L. LISTER,¹⁸ R. MAIOLINO,¹⁹ W. MAX-MOERBECK,²⁰ B. MOLINA,² P. MRÓZ,²¹ C. P. O'DEA,^{22,23} V. PAVLIDOU,^{4,1} T. J. PEARSON,⁶ M.F. ALLER,²⁴ C. R. LAWRENCE,²⁵ T. J. W. LAZIO,²⁵ S. O'NEILL,²⁶ T. A. PRINCE,⁷ V. RAVI,⁶ R.A. REEVES,² K. TASSIS,^{4,1} M. VALLISNERI,²⁵ AND J. A. ZENSUS²⁷

¹*Institute of Astrophysics, Foundation for Research and Technology-Hellas, GR-71110 Heraklion, Greece*

²*CePIA, Astronomy Department, Universidad de Concepción, Casilla 160-C, Concepción, Chile*

³*Kavli Institute for Particle Astrophysics and Cosmology, Department of Physics, Stanford University, Stanford, CA 94305, USA*

⁴*Department of Physics and Institute of Theoretical and Computational Physics, University of Crete, 71003 Heraklion, Greece*

⁵*NASA Marshall Space Flight Center Huntsville, AL 35808, USA*

⁶*Owens Valley Radio Observatory, California Institute of Technology, Pasadena, CA 91125, USA*

⁷*Division of Physics, Mathematics, and Astronomy, California Institute of Technology, Pasadena, CA 91125, USA*

⁸*JILA, University of Colorado and National Institute of Standards and Technology, 440 UCB, Boulder, CO 80309-0440, USA*

⁹*Department of Astrophysical and Planetary Sciences, 391 UCB, Boulder, CO 80309-0391, USA*

¹⁰*Cavendish Laboratory, University of Cambridge, 19 JJ Thomson Avenue, Cambridge, CB3 0HE, UK*

¹¹*Department of Physics and Astronomy, University College London, Gower Street, London WC1E 6BT, UK*

¹²*Department of Physics, California Institute of Technology, Pasadena, California 91125, USA*

¹³*LIGO Laboratory, California Institute of Technology, Pasadena, California 91125, USA*

¹⁴*Cahill Center for Astronomy and Astrophysics, California Institute of Technology, Pasadena, CA 91125, USA*

¹⁵*Department of Physics and Astronomy, Denison University, Granville, OH 43023, USA*

¹⁶*Finnish Centre for Astronomy with ESO (FINCA), University of Turku, FI-20014 University of Turku, Finland*

¹⁷*Aalto University Metsähovi Radio Observatory, Metsähovintie 114, 02540 Kylmälä, Finland*

¹⁸*Department of Physics and Astronomy, Purdue University, 525 Northwestern Avenue, West Lafayette, IN 47907, USA*

¹⁹*Kavli Institute for Cosmology, University of Cambridge, Madingley Road, Cambridge, CB3 0HA, UK*

²⁰*Departamento de Astronomía, Universidad de Chile, Camino El Observatorio 1515, Las Condes, Santiago, Chile*

²¹*Astronomical Observatory, University of Warsaw, Al. Ujazdowskie 4, 00-478 Warszawa, Poland*

²²*Department of Physics and Astronomy, University of Manitoba, Winnipeg, MB R3T 2N2, Canada*

²³*Center for Space Plasma & Aeronomic Research, University of Alabama in Huntsville, Huntsville, AL 35899 USA*

²⁴*Department of Astronomy, University of Michigan, 323 West Hall, 1085 S. University Avenue, Ann Arbor, MI 48109, USA*

²⁵*Jet Propulsion Laboratory, California Institute of Technology, 4800 Oak Grove Drive, Pasadena, CA 91109, USA*

²⁶*Department of Physics, Princeton University, Jadwin Hall, Princeton, 08540, NJ, USA.*

²⁷*Max-Planck-Institut für Radioastronomie, Auf dem Hügel 69, D-53121 Bonn, Germany*

ABSTRACT

Haystack and Owens Valley Radio Observatory (OVRO) observations recently revealed strong sinusoidal total flux density variations that maintained coherence between 1975 and 2021 in the blazar PKS 2131–021 ($z = 1.283$). This was interpreted as possible evidence of a supermassive black hole binary (SMBHB). Extended observations through 2023 show coherence over 47.9 years, with an observed period $P_{15\text{ GHz}} = (1739.3 \pm 1.2)$ days. We reject, with p -value $= 5.3 \times 10^{-7}$, the hypothesis that the variations are due to random fluctuations in the red noise tail of the power spectral density. There is clearly a constant-period physical phenomenon in PKS 2131–021 producing coherent intermittent sinusoidal flux density variations. We find the coherent sinusoidal intensity variations extend from below 2.7 GHz to optical frequencies, from which we derive an observed period $P_{\text{optical}} = (1764 \pm 36)$ days. Across this broad frequency range there is a monotonic phase shift in the sinusoidal variations with frequency. The same coherent periodicity is possibly also observed at γ -ray energies. The importance of well-vetted SMBHB candidates to searches for gravitational waves is pointed out. We estimate the fraction of blazars that are SMBHB candidates to be > 1 in 100. Thus monitoring programs covering tens of thousands of blazars could discover hundreds of SMBHB candidates.

Keywords: galaxies: active, galaxies: relativistic jets, quasi-periodic oscillators

1. INTRODUCTION

The 40 m Telescope of the Owens Valley Radio Observatory (OVRO) has been engaged in monitoring the total 15 GHz flux densities of ~ 1830 blazars since 2008 (Richards et al. 2011) on a 3–4 day cadence. The first statistically robust report of a strong supermassive black hole binary (SMBHB) candidate (PKS 2131–021) showing sinusoidal variations in its radio light curve was presented by O’Neill et al. (2022, hereafter Paper 1).

SMBHBs are a direct result of hierarchical structure formation and an important ingredient for our understanding of the evolution of the Universe (e.g., Volonteri et al. 2003; Maiolino et al. 2023; Übler et al. 2024). In spite of the significant effort that has been put into finding SMBHBs (see D’Orazio & Charisi 2023, for a recent review), the number of compelling candidates remains small. This is particularly true for blazars, active galactic nuclei (AGN) with jets oriented toward the observer on Earth (Blandford et al. 2019; Hovatta & Lindfors 2019). Until recently, the most compelling blazar SMBHB candidate with a separation $\ll 1$ pc had been OJ 287, identified through more than 100 years of optical observations showing an outburst every ~ 11 years due to the secondary black hole crossing the accretion disk of the primary (Sillanpää et al. 1988; Valtonen et al. 2016; Dey et al. 2021). All-sky surveys in optical and γ -rays have produced more candidates (e.g., PG 1302–102, Graham et al. 2015; PG 1553+113, Ackermann et al. 2015), and future facilities like the Vera C. Rubin observatory are expected to produce many more (e.g., Xin & Haiman 2021).

In the radio regime, periodicity searches have been limited because of the scarcity of facilities capable of regularly observing a large number of blazars. The Owens Valley Radio Observatory 40-m Telescope blazar program (Richards et al. 2011) is currently the largest radio flux-density monitoring program. Given the quality and length of the OVRO light curves, we have engaged in a search for statistically significant periodic and quasi-periodic oscillations (QPOs). In Paper 1 we presented our first results on PKS 2131–021, providing evidence of a periodicity in this blazar. These results showed that the observed periodicity is highly unlikely to be due to random fluctuations and the red noise tail in the variability spectrum. In view of the stability of its period, PKS 2131–021 is a strong SMBHB candidate. In this paper, we present further evidence, which we find compelling, supporting the hypothesis of the SMBHB nature of PKS 2131–021.

We analyze the radio to optical light curves of PKS 2131–021 in terms of a model due to Blandford (see Paper 1), which ascribes the sinusoidal variations in PKS 2131–021 to aberration caused by the orbital motion in an SMBHB of the SMBH producing the jet. This same model had been developed by Sobacchi et al. (2017) in the context of a “spine-sheath” model, but we missed the underlying similarity. We will refer to this as the “Kinematic Orbital” model (KO model).

As discussed in Paper 1, blazars showing evidence of periodicities should not be considered bona fide periodic or quasi-periodic oscillator (QPO) candidates unless it can be shown that there is a very low *global* probability (p -value $< 1.3 \times 10^{-3}$), taking into account the look-elsewhere effect, that the periodicity is due to red noise tail fluctuations, through a careful analysis of the power spectral density (PSD) and through simulations that reproduce both the observed PSD and the observed probability density function (PDF) seen in the light curve. Such analysis is essential for assessing the chance occurrence probability of sinusoidal features in light curves of AGN.

The factors supporting the hypothesis that the blazar PKS 2131–021 is an SMBHB, based on 15 GHz light curves from the Haystack and Owens Valley Radio Observatories up to 2021, were presented in Paper 1. In this paper, we present new 15 GHz data that confirm predictions based on observations obtained up to 2021, and show that there is no need to “adjust” the model: the new OVRO data match the model predictions *without altering its original parameters*, thereby fulfilling a classic test of a scientific model.

We also analyze the light curves of PKS 2131–021 at 2.7 GHz, 7.9 GHz, 15.5 GHz and 31.4 GHz using Haystack observations from 1975–1983 (O’Dea et al. 1986), 15 GHz observations from OVRO, and ALMA observations at 91.5 GHz, 104 GHz, and 345 GHz. In addition, we analyze infrared data from WISE, optical data from the Zwicky Transient Facility (ZTF), and γ -ray data from the Fermi Gamma-ray Space Telescope, and show that sinusoidal variations, coherent with the radio variations, are clearly seen at optical wavelengths, and, furthermore, hints of coherent periodic variations are seen at both infrared wavelengths and γ -ray energies.

This paper is organized as follows: in Section 2 we discuss the continuation of the 15 GHz sinusoidal variations in PKS 2131–021 for another 2 yr; in Section 3 we discuss the radio spectrum, structure, and polarization of PKS 2131–021 to provide background for the later sec-

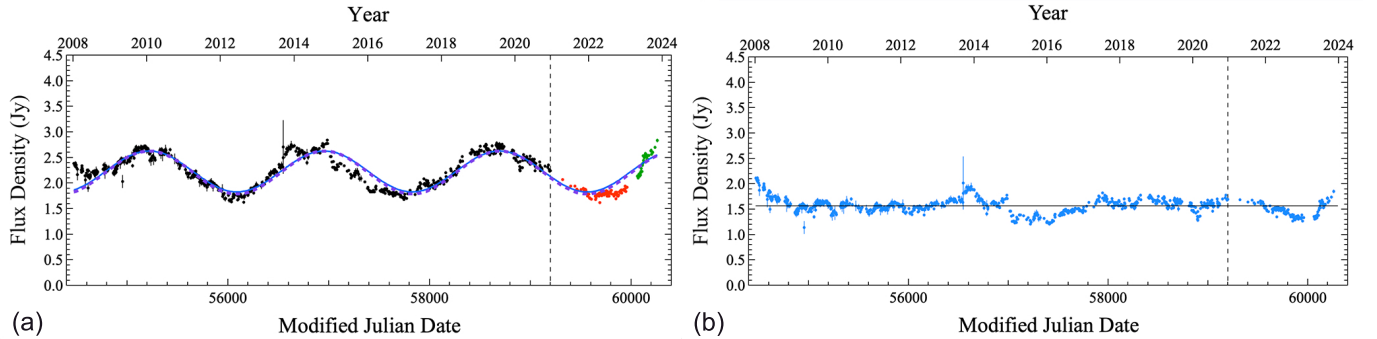


Figure 1. Verified prediction in the 15 GHz light curve of PKS 2131–021. (a) Black points: The OVRO 15 GHz light curve presented in Paper 1, which extends up to the vertical dashed line; blue curve: the least-squares sine-wave fit to the Haystack+OVRO data given in Table 1 of Paper 1, extrapolated to the end of 2023. Note the divergence of the data (red points) from the fit. The prediction at this point was that the light curve would revert to the sine wave. The more recent 2023 observations (green points) show that the observed curve has returned to the extrapolated fit (blue curve), as predicted in Paper 1. The purple dashed sine curve, which is almost indistinguishable from the blue sine curve, is the best least squares fit, given in Table 1, to the Haystack data plus all of the OVRO data to the end of 2023. (b) The residual 15 GHz light curve after subtraction of the sinusoidal component (purple dashed sine wave) plotted in (a). The black horizontal line indicates the mean flux density in the residual.

tions; in Section 4 we present evidence that strong coherent sinusoidal variations are seen from 2.7 GHz to optical frequencies, with a monotonically varying phase shift as a function of frequency; in Section 5 we discuss the X-ray observations of PKS 2131–021 and the prospects for future X-ray observations; in Section 6 we discuss the γ -ray emission from PKS 2131–021; in Section 7 we discuss the multifrequency observations in terms of the KO model; in Section 8 we discuss the fraction of blazars that are SMBHB candidates; in Section 9 we summarize our findings and discuss their implications. There are three appendices: in Appendix A we discuss the Doppler factor for the compact radio component; in Appendix B we discuss the implications of the absence of higher harmonics in the light curve; in Appendix C we discuss the determination of the parameters of the sinusoidal optical light curves.

For consistency with our other papers, we assume the following cosmological parameters: $H_0 = 71 \text{ km s}^{-1} \text{ Mpc}^{-1}$, $\Omega_m = 0.27$, $\Omega_\Lambda = 0.73$ (Komatsu et al. 2009). None of the conclusions would be changed were we to adopt the best model of the Planck Collaboration (Planck Collaboration et al. 2020).

2. THE CONTINUATION OF THE 15 GHz SINE WAVE SIGNAL IN PKS 2131–021

The OVRO 15 GHz light curve of PKS 2131–021 is shown in Fig. 1, where the vertical dashed line marks the extent of our calibrated data (up to MJD 59197) analyzed in Paper 1. The sine-wave fitting method is described in Paper 1. In Fig. 1(a) the blue curve shows the least squares sine wave fit to the data prior to MJD 59197 (black points) extrapolated forward to the end of

2023 (MJD 60310). As can be seen, by mid-January 2023 (MJD 59959) the new data appeared at first to be diverging from the extrapolated sine curve (red points), but they returned to it in 2023 (green points), thus fulfilling the prediction, from Paper 1, of a constant long-term period. The observed 47.9 year continuity, when combined with the Haystack data, is unprecedented in the light curves of blazars. In Fig. 1(b) we show the residual variations in PKS 2131–021 after subtraction of the sinusoidal component.

The combination of the Haystack and OVRO 15 GHz data is shown in Fig. 2, together with two sine-wave fits. Between these two epochs the sinusoidal variation disappeared (see Paper 1). In Fig. 2(a) we show a sine-wave fit in which each data point is given equal weight. While the fit is quite good, it is clear that there is a slight offset in phase between the sine wave and the Haystack data. The Haystack data are particularly relevant with respect to any phase offsets because of the long time interval of 25 years that separates them from the OVRO data. For the purpose of determining the underlying periodicity, and hence the degree of coherence in the combined data set, in Fig. 2(b) we have assigned a weight of $879/154 = 5.71$ to each of the Haystack observations, corresponding to the number of data points in the Haystack data (154) and the OVRO data (879). The weights of the OVRO data points are all 1. As can be seen in Fig. 2(b), this has brought the sine wave into alignment with the Haystack data, with no discernible difference in the fit to the OVRO data. The corresponding period is $P = (1739.2 \pm 1.2)$ days, which may be compared with the period of $P = (1737.9 \pm 2.6)$ days obtained in Paper 1. The period in the $z = 1.283$ rest frame of

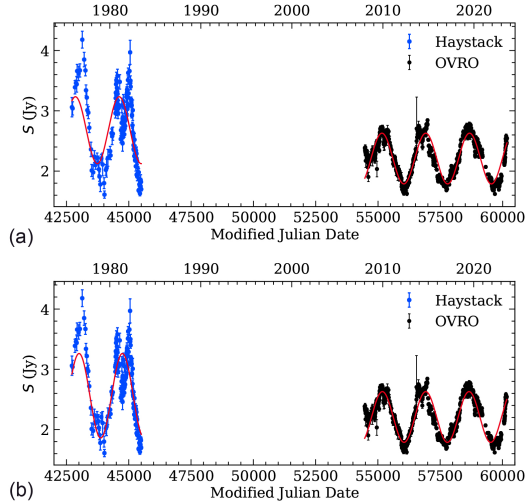


Figure 2. Sine wave fits (red curves) to the combined Haystack observations from 1975 to 1983 (O’Dea et al. 1986) and OVRO observations from 2008 to the end of 2023. The amplitudes have been permitted to vary between the two data sets, but the period is derived from the combined data set. (a) Fit to the unweighted data. (b) Fit in which the Haystack observations have been assigned weights of $w = 879/154 = 5.71$, where 879 and 154 are the numbers of data points in the OVRO and Haystack light curves, respectively (see text).

the host galaxy is $P_0 = 762 \pm 0.5$ days. As discussed in Paper 1, the cause of the difference in the amplitudes of the sine waves in the Haystack data and the OVRO data is unknown.

We have used the above best estimate of the period, $P = (1739.2 \pm 1.2)$ days, as a prior in determining the best fitting sine wave to the OVRO data. The resulting parameters are given in Table 1, and the corresponding sine wave is shown by the purple dashed sine wave in Fig. 1(a).

Table 1. The Best Least Squares OVRO Sine Wave

Parameter	Value
P (days)	$1739.2 \pm 1.2(\text{prior})$
ϕ_0 (rad)	-0.084 ± 0.016
A (Jy)	0.4195 ± 0.0066
S_0 (Jy)	2.2084 ± 0.0046
σ_0 (Jy)	0.1227 ± 0.0034

NOTE—The period is that of the Haystack+OVRO data with the weights in the ratio of the number of data points ($879/154 = 5.71$) shown by the red sine wave in Fig. 2(b). This period is used as a prior in obtaining the parameters above for the best least squares sine wave fit to the OVRO data shown by the purple dashed curve in Fig. 1(a).

2.1. Statistical Significance of the Sinusoid Parameter Agreement in 1975–1981 vs. 2008–2023

We carried out the generalized Lomb–Scargle (GLS) (Lomb 1976; Scargle 1982) periodogram analysis described in Section 3.4 of Paper 1. With this analysis we address the question whether a random process can spuriously produce the detected periodic signals in the OVRO and Haystack data. The Null hypothesis is that the light curves originate from a power-law red noise process that reproduces the power spectral density (PSD) and probability density function (PDF). We devise three tests.

Test 1 – OVRO data: Under the Null hypothesis, what is the probability that the strongest peak in the GLS periodogram has a higher test statistic than the GLS peak of the the OVRO data? The test statistic is the significance of the GLS peak estimated at the peak frequency. We refer to Appendix A of Paper 1 for a detailed description of the procedure. Based on 300,000 simulations we estimate a probability of $= 1.33 \times 10^{-4}$ (3.65σ).

Test 2 – Haystack data period: Under the Null hypothesis and knowing the period in the OVRO data, what is the probability that the strongest peak in the GLS periodogram of the Haystack data (a) has a power of at least 0.5 and (b) appears at a period in the 3σ -uncertainty range spanning the period detected in the OVRO data? Based on 100,000 simulations we estimate a probability of $= 1.97 \times 10^{-2}$ (2.06σ).

Test 3 – Haystack data phase: Under the Null hypothesis, and assuming the Haystack data shows a periodicity with period matching that of the OVRO data, what is the probability that the phases match to within 20% of a half-period? In the case of a randomly produced spurious periodicity, the phase would be uniformly distributed. Therefore, the probability for test 3 is 0.2.

We estimate the probability of all three observations as defined in tests 1–3 under the Null hypothesis by multiplying the probabilities of the three independent tests. The joint probability is 4.25×10^{-7} (4.88σ). All tests and results are summarized in Table 2.

We reject the Null hypothesis at $> 3\sigma$ significance level based on the OVRO data alone, and with much higher confidence based on the joint results from the OVRO and Haystack data analysis. It is highly unlikely that a random process spuriously produced the observed periodicity. Consequentially, a different, non-random process must have produced the periodic signal.

These results provide compelling evidence that there is a long-term persistent periodic physical phenomenon in PKS 2131–021 that, given the 19-year gap in the

Table 2. Probabilities and Significance Levels of GLS Tests Computed from Simulations with Matched Red Noise Tail

Test Number	Test	GLS $\mathcal{P}_{\text{peak}}$ (max=1)	Period Range (ΔP) (days)	Total Simulations	Number of simulations that pass test	p-value	Significance (σ)
1	OVRO data	0.81	All	300000	40	1.33×10^{-4}	3.65
2	Haystack data	≥ 0.50	1657.5 – 1854.1	10000	197	1.97×10^{-2}	2.06
3	phase	-	-	-	-	0.2	0.8
-	Combining 1, 2 and 3	-	-	-	-	5.25×10^{-7}	4.88

NOTE— \mathcal{P} is the GLS power and ΔP is the range of periods included in the test. The tests are described in Sec. 2.1.

sinusoidal variations from 1984 to 2003, produces intermittent sinusoidal variations in its light curve. In our view it is highly likely, based on the 15 GHz observations alone, that the variations are due to the orbital motion of a jet-producing SMBH in an SMBHB.

3. THE RADIO SPECTRUM, STRUCTURE, AND POLARIZATION OF PKS 2131–021

The radio spectrum of PKS 2131–021, as measured from centimeter to sub-millimeter wavelengths by the Planck observatory at eight different epochs (Rocha et al. 2023), is shown in Fig. 3. Below 30 GHz the spectrum continues flat all the way down to 100 MHz (NASA/IPAC NED). It is somewhat unusual for a blazar to have a flat radio spectrum all the way from 100 MHz to 70 GHz. This is indicative of a very compact jet structure. Above 70 GHz, the emission transitions from optically thick to optically thin, and the spectrum steepens to a spectral index $\alpha = -0.74$, and then above 350 GHz it flattens again—possibly due to the ejection of a new jet component.

The flat radio spectrum of PKS 2131–021 from < 100 MHz to 70 GHz must be due to synchrotron self-

absorption (Scheuer & Williams 1968), with the lower-frequency radiation coming from further out along the jet than the higher-frequency radiation, as is common in blazar sources with “core-jet” morphologies, such as PKS 2131–021 (Readhead et al. 1978; Readhead 1980).

The centimeter-wavelength single-dish linear polarization of PKS 2131–021 was monitored by the University of Michigan Radio Astronomy Observatory (UMRAO), where the source showed a fairly low typical fractional polarization of 2.8% at 14.5 GHz (Aller et al. 1999). The source was also included in the VLBA polarization monitoring program by Gabuzda et al. (2000).

Figure 4 shows the stacked-epoch VLBA total intensity (left panel) and polarization (right panel) images of PKS 2131–021 at 15 GHz from the MOJAVE program (Pushkarev et al. 2023). The epochs that have been stacked are shown at the top of the figure. We see that PKS 2131–021 has the typical “core-jet” structure common to blazars.

The polarization image of Fig. 4 is produced by first averaging the total intensity I and Stokes parameters Q and U over the 16 observing epochs between 1997 and 2012, and then calculating the fractional polarization and electric vector position angle (EVPA) images from the stacked quantities (see Pushkarev et al. 2023, for details). Stacking the polarization this way reveals the underlying magnetic field structure. It also reveals a much broader cross-section of the entire jet, which is not often fully visible at individual epochs.

The EVPA vectors shown on the right in Fig. 4 indicate that the electric field is predominantly parallel to the jet direction, assuming that the Faraday rotation in the jet is small, as was shown in Hovatta et al. (2012). The only exception to this is the region south-east from the core, which is due to a single component (component 3, see Paper 1), showing a transverse polarization structure. Predominantly parallel EVPA in an optically thin jet, as in this source (Hovatta et al. 2014), means that the underlying magnetic field is dominated by a toroidal component.

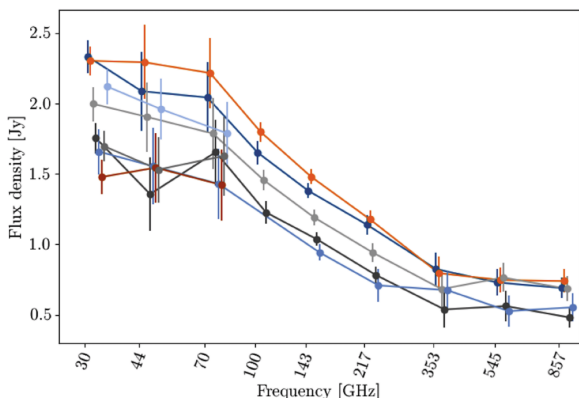


Figure 3. The radio spectrum of PKS 2131–021 from centimeter to sub-millimeter wavelengths measured by the Planck observatory at eight different epochs (Rocha et al. 2023).

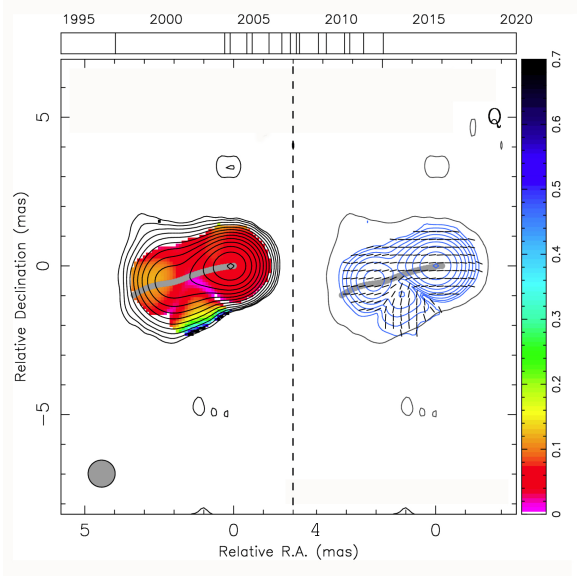


Figure 4. Stacked polarization image of PKS 2131–021 at 15 GHz from the MOJAVE program (Pushkarev et al. 2023). The left panel shows the stacked total intensity emission over the 16 epochs between 1997 and 2012 in contours, while the color scale indicates the amount of fractional polarization. The right panel shows the lowest total intensity contour (black) and polarized intensity contours (blue) along with the direction of the EVPA (black tick marks). The gray curve shows the ridge line in total intensity. The timeline on the top of the image indicates the observing epochs by vertical lines.

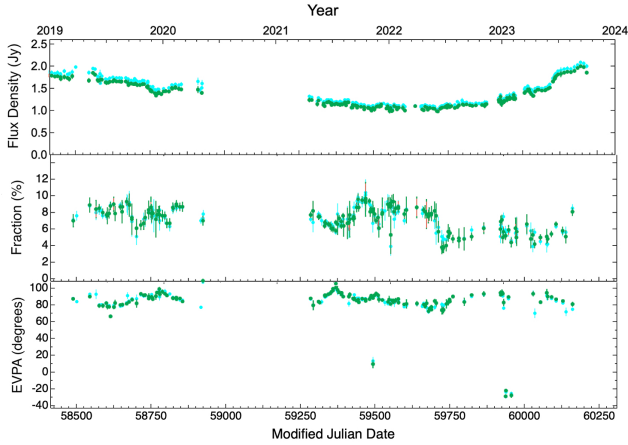


Figure 5. Polarization of PKS 2131–021 observed in ALMA Band 3 (Cyan points: 91.5 GHz; green points: 103.5 GHz.). The EVPA changes little, if at all, between 15 GHz and 345 GHz, and shows no dramatic shift between the optically thick and optically thin regimes.

The integrated linear polarization in PKS 2131–021 stays predominantly parallel to the jet direction all the way up to 350 GHz (Rocha et al. 2023). As described

in section 4.1, PKS 2131–021 is an ALMA calibrator, and we have used that data extensively in this paper. The variation in the linear polarization at 91.5 GHz and 103.5 GHz from 2019 to 2023.5 seen by ALMA is shown in Fig. 5, where it is seen that the EVPA changes little throughout the sinusoidal cycle.

These linear polarization observations show that the magnetic field in PKS 2131–021 is dominated by the helical component B_ϕ , and that there must be a strong current, I , along the jet.

Circular polarization observations of PKS 2131–021 are also available from the MOJAVE program. In the first epoch of MOJAVE observations in May 2003, no significant circular polarization was detected; the upper limit on the fractional circular polarization was $m_c < 0.19\%$ (Homan & Lister 2006). This is typical behavior at 15 GHz, where only 17 out of 133 sources in the single-epoch study of Homan & Lister (2006) showed significant circular polarization detections at higher than 3σ level. However, in a multi-epoch study covering all MOJAVE data until the end of 2009, the source is detected in circular polarization with $m_c = (-0.456 \pm 0.095)\%$ during one epoch in February 2009 (Homan et al. 2018). During this epoch, the linear polarization of the core component reaches its highest level $m_l = 7.0\%$ within the MOJAVE epochs analyzed until the end of 2009. As discussed in Homan et al. (2018), it is not unusual for a source to show significant circular polarization at single epochs, and 91 out of the 278 sources showed a significant detection at least during one observing epoch, with typical detection levels being in the range 0.3–0.7%. The source was also observed at 15, 22, and 43 GHz by Vitriishchak et al. (2008), but only upper limits on circular polarization were derived with limits of $< 0.24\%$, $< 0.70\%$, and 0.78% at 15, 22, and 43 GHz, respectively.

Circular polarization can be due either to intrinsic circular polarization of the synchrotron emission or to Faraday conversion of linear to circular polarization (e.g., Jones & O’Dell 1977). At centimeter wavelengths, it is often attributed to Faraday conversion (e.g., O’Sullivan et al. 2013), although in the inhomogeneous VLBI cores it can also be due to intrinsic circular polarization (Homan et al. 2009). With only single frequency observations it is impossible to distinguish between the two scenarios.

4. THE CENTIMETER-TO-OPTICAL EMISSION IN PKS 2131–021

4.1. The Centimeter-to-Submillimeter Emission

The Haystack observations from 1975 to 1983 at 2.7, 7.9, 15.5, and 31.4 GHz (O’Dea et al. 1986) are shown

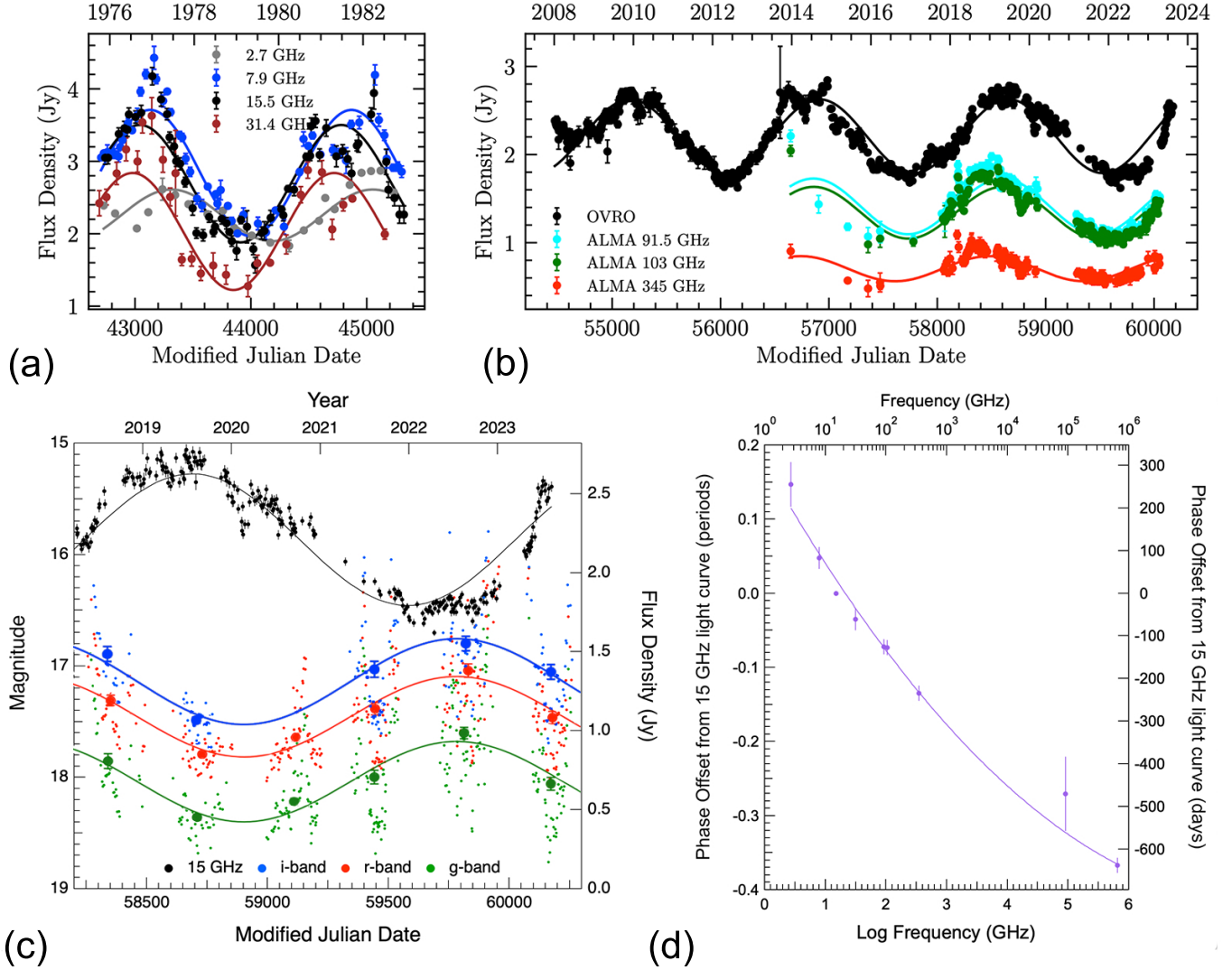


Figure 6. PKS 2131-021 light curves at radio, mm, sub-mm, and optical wavelengths showing a steady monotonic progression of the phase of the sinusoidal variations with frequency. (a) Haystack 2.7–31.4 GHz observations (O’Dea et al. 1986) together with the least-squares sine-wave fits to the data at each of the frequencies. There is a steady progression in phase with frequency between the four light curves, with the low-frequency sine waves lagging the high-frequency sine waves. (b) OVRO 15 GHz light curve plus ALMA light curves at 91.5, 104, and 345 GHz. As in (a), there is a continuing progression in the phases of the sine wave fits with frequency. (c) Comparison of the ZTF optical and OVRO radio light curves of PKS 2131-021. The ZTF *i*, *r*, and *g*-band light curves of PKS 2131-021 are shown. The large symbols are average values for each year. The black points show the OVRO 15 GHz points over this period, which provide the phase reference point. The curves show the least squares sine wave fits to the corresponding data. We associate the optical peak with the *nearest* radio peak, not the preceding radio peak. (d) The observed phase shifts, relative to the OVRO 15 GHz light curve, of the sine-wave fits to the data, given in Table 3. A positive phase shift indicates that the light curve is shifted to a later time than the 15 GHz light curve. The curve shows a quadratic polynomial fit to the phase offset *vs.* log(frequency) data (see Sect. 4.3).

in Fig. 6(a), and the OVRO and ALMA lightcurves between 2008 and 2023 at 15, 91.5, 104, and 345 GHz are shown in Fig. 6(b). The ALMA data were downloaded from the ALMA calibrator website. The color-coded curves are least-squares fits of sine waves to the data, derived by the procedure presented in Paper 1. The phase offsets derived from the sine-wave fits of Figs. 6(a) and (b) are given in Table 3. The 15.5 GHz (Haystack)

and 15 GHz (OVRO) light curves were used as reference light curves, since these frequencies occur in the earlier lower-frequency and the later higher-frequency data sets, respectively, and these frequencies are essentially the same to the accuracy needed here. Note that the phase shifts vary monotonically with frequency from the lowest to the highest frequency of observation, i.e. from 2.7 GHz to the optical band. To the best of our

Table 3. Phase Shift with Frequency Relative to the 15 GHz Light Curve

Frequency Band	Phase (Fraction of a cycle)	Uncertainty (Fraction of a cycle)
2.7 GHz	0.147	0.03
7.9 GHz	0.048	0.015
15 and 15.5 GHz	0	0
31.4 GHz	−0.035	0.015
91.5 GHz	−0.072	0.01
104 GHz	−0.073	0.01
345 GHz	−0.135	0.01
infrared	−0.27	0.05
Optical	−0.37	0.01

NOTE—The 15.5 GHz light curve was observed in 1975–1983, and the 15 GHz light curve was observed in 2008–2023), so these were used as the phase reference in both the Haystack data and the OVRO+ALMA data. The infrared and optical light curves are referred to the 15 GHz OVRO light curve.

knowledge, such coherence in the flux density variations in a blazar, extending from the radio band to the optical band, has not been observed before.

4.2. The Infrared to Optical Emission in PKS 2131–021

4.2.1. The 2.8 μ m–5.2 μ m emission

We have extracted the Wide Field Infrared Explorer (WISE) data in the 2.8–3.8 micron and 4.1–5.2 micron bands. In Paper 1 we carried out a cross-correlation analysis of the WISE 1 (2.8–3.8 μ m) and WISE 2 (4.1–5.2 μ m) data with the OVRO 15 GHz light curve and found marginal ($\sim 2\sigma$) evidence for a correlation. The WISE data are very sparsely sampled in time and in our cross-correlation analysis of the complete data set the peak cross correlation significance is less than 2σ . However we find that the phase of the WISE 1–OVRO cross-correlation data, relative to the OVRO 15 GHz light curve, is -470^{+166}_{-147} days, and that of the WISE 2 data is -470^{+177}_{-162} days (i.e., $-0.27^{+0.10}_{-0.09}$ of the period in both cases).

The cross-correlation between the OVRO and WISE data was performed following Max-Moerbeck et al. (2014). The uncertainty in the delay is derived using 1000 iterations of ‘random subset selection’ and ‘flux randomization’ as described in Peterson et al. (1998). Since the WISE data are so sparse, it was necessary to

fit the position of the cross-correlation peak because it was not always well defined and showed large fluctuations. The fit was done using a parabola and included the cross-correlation delays from -1000 to 0 days. The quoted intervals correspond to 1σ error bars.

The data we have suggest, therefore, that the sinusoidal signal is present in the infrared WISE bands.

4.2.2. Strong Optical Sinusoidal Emission

In Paper 1 we reported that the optical variations in PKS 2131–021 observed with the Zwicky Transient Facility (ZTF; Graham et al. 2019; Masci et al. 2019) were not correlated with the 15 GHz variations. The optical data in Paper 1 extended to 2021 Oct 1 and spanned only about half of a single period in the sinusoidal variations. We have now added another two years of ZTF data up to 2023 Sep 9, so that, all told, the ZTF data now span a full period. We now find that there is a *strong* sinusoidal variation at optical wavelengths of the same frequency as that in the 15 GHz light curve.

The ZTF *g*, *r*, and *i* band light curves of PKS 2131–021 (Fig. 6c) show a periodic variation having the same period, to within the uncertainties, as the 15 GHz light curve. Sine-wave fits to the ZTF data are presented in Appendix C. where we show that the combined sine-wave fit to all three data sets yields a period of $P_{\text{optical}} = (1764 \pm 36)$ days. This agrees, within the uncertainties, with the period of (1739.2 ± 1.2) days determined from the OVRO+Haystack data. It appears, therefore, that the sinusoidal variations persist at least up to optical wavelengths. We present evidence below that the same periodicity likely continues up to γ -ray energies. The time shift between the observed maxima in the sine wave fits to the optical light curves and the 15 GHz curve is 638 or 1101 days, depending on the direction of the shift. The more obvious choice is 638 days, since this shifts the light curve in the same direction relative to the 15 GHz OVRO light curve as we determined from cm to sub-mm wavelengths, and continues the monotonic trend we have observed at the lower frequencies (see Fig. 6(d)). We return to this point in section 6.

4.2.3. The Comparative Difficulty of Detecting Optical vs. Radio Sinusoidal Variations in Blazars

This is the first detection of statistically compelling sinusoidal variations in a blazar at both optical and radio wavelengths. It provides the opportunity to estimate the relative difficulty of making such detections in these two windows. As shown in Paper 1, the peak random fractional variations in the radio light curve are $\sim 20\%$ (see Fig. 10(c) of Paper 1). From the ZTF data of Fig. 6(c) we find that the peak random fractional vari-

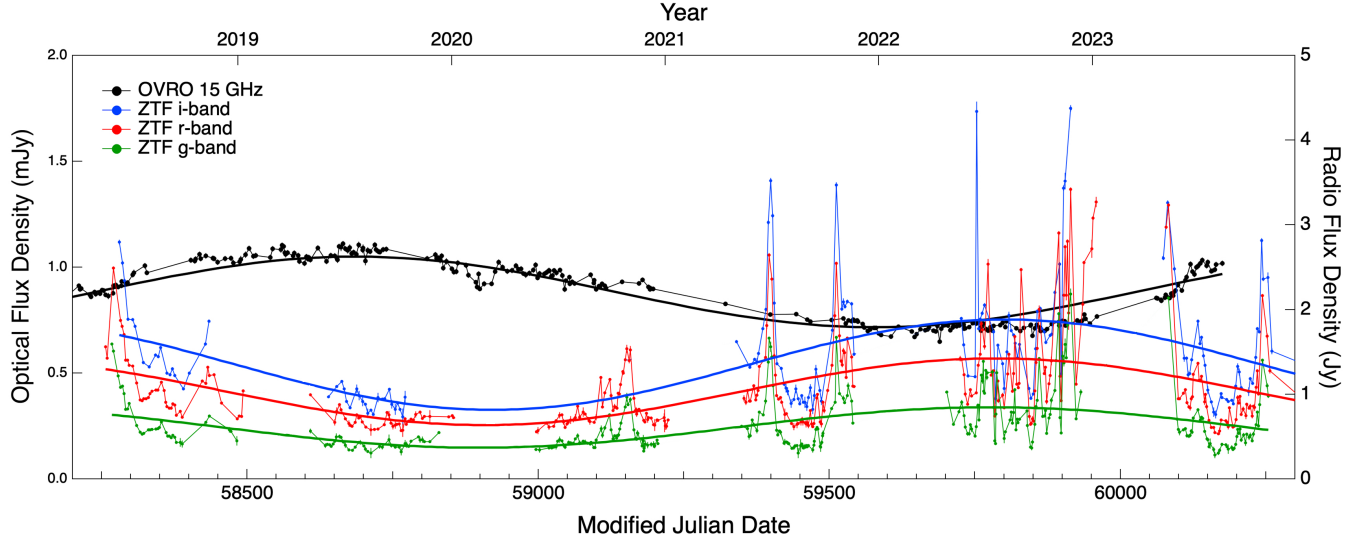


Figure 7. Comparison of the short-term random variations in PKS 2131–021 at radio and optical wavelengths *vs.* the sinusoidal variations in these two windows. The flux density scales have been adjusted such that the amplitudes of the radio and optical sine waves are approximately equal, in order to be able to compare the amplitudes of the short term variations at optical and radio frequencies. In general the radio short-term variations are significantly smaller than those at optical wavelengths (see text).

ations in the optical light curve are $\sim 200\%$. This order of magnitude difference, coupled with the extraordinary challenges of determining the high statistical significance of the sinusoidal variations in PKS 2131–021, with all the various types of confusion that are introduced by the random variations discussed in Paper 1 and the inevitable annual gaps in the optical light curves, reveals that the detection of statistically significant optical sinusoidal variations in blazars is a daunting challenge. The situation is illustrated in Fig. 7. There are periods when the optical short-term variations are no larger than those at radio wavelengths, but there are also periods when they are an order of magnitude, or more, greater than those at radio wavelengths, making it more difficult to detect sinusoidal variations at optical than at radio wavelengths.

It is clear that, in optical searches for sinusoidal blazar variations, a minimum of *both* ~ 100 observations per year *and* rigorous statistical red noise tests for global significance are needed to detect sinusoidal variability in blazars with periods of several years. Without such dense sampling and rigorous statistical testing there is a high probability of spurious detections of sinusoidal periodicities in blazars at *both* radio *and* optical wavelengths.

In order to obtain a qualitative measure of the relative difficulty of detecting a blazar showing sinusoidal variations like those seen in PKS 2131–021 at optical and radio wavelengths, we have carried out the same GLS analysis on the optical data as on the radio data, using

the optical data shown in Fig. 7. We found that the local p -values of the GLS peaks in the i , r , and g bands are 0.5, 0.4, and 0.5, respectively, whereas that at 15 GHz is 0.002.

4.3. Coherence of the Periodicity from the Radio to the Optical Emission

The phase shifts measured in the previous sections are tabulated in Table 3 and plotted in Fig. 6(d). They are well-fitted by a linear-logarithmic fit, as shown on the linear-log plot of Fig. 6(d). A linear fit to the 2.7 GHz – 345 GHz data is given by

$$\delta\phi = 0.024 - 0.125 \log_{10}(\nu/15) \quad (1)$$

where ν is in GHz. We make use of this relationship in equation (3) below. The curved line of Fig. 6(d) shows a quadratic polynomial fit to all the data given by $\delta\phi = 0.176 - 0.144 \log_{10}(\nu/15) + 0.0087[\log_{10}(\nu/15)]^2$.

The monotonic variation in phase lag with frequency from 2.7 GHz to optical frequencies demonstrates convincingly that the sinusoidal variation is caused by a physical process in the source.

4.4. The Fractional Amplitude of the Sinusoidal Variations

In Fig. 8 we show the fractional amplitudes of the sine wave fits to the Haystack, OVRO, ALMA, WISE and ZTF data (i.e., the sine-wave amplitudes divided by the mean flux). The fractional amplitude of the sine wave observed between 1975 and 1983 at Haystack

is clearly dropping at the lowest frequency (2.7 GHz). The blue points (OVRO+ALMA) and the black point (ZTF) have considerably more data than the green points (Haystack) and the WISE data.

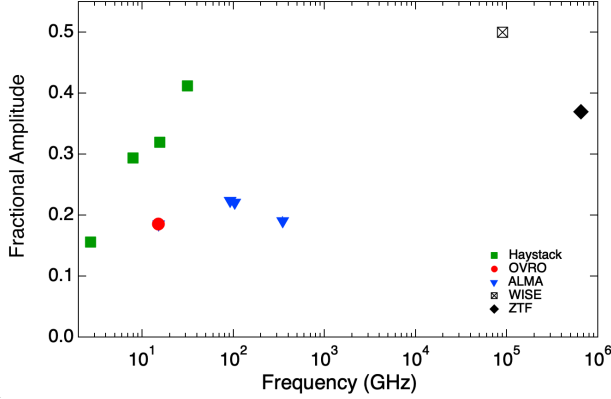


Figure 8. Fractional amplitudes of the fitted sine waves as a function of frequency. The amplitudes are normalized by the mean amplitude of each light curve. The data displayed are: Haystack data, from 1975 to 1983 (green squares), OVRO (red circle) and ALMA (blue points) data from 2014 to 2023, the ZTF data (black diamond), and the measured fractional amplitude of the variations in the WISE data (black crossed square). In all cases the error bars are smaller than the symbols.

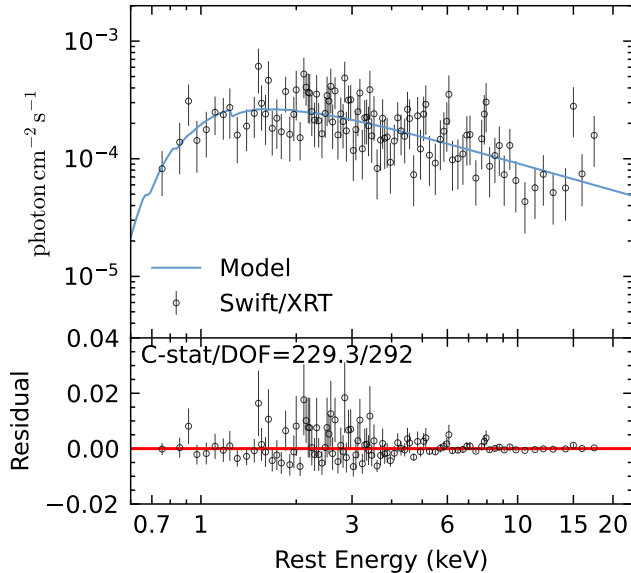


Figure 9. Stacked *Swift*/*XRT* spectrum of PKS 2131–021 shifted to the rest frame of $z = 1.283$. The spectrum is characterized by an absorbed powerlaw with photon index $\Gamma = 1.78 \pm 0.15$ and rest frame hydrogen column density $N_{\text{H}} = 3.4^{+2.7}_{-2.4} \times 10^{21} \text{ cm}^{-2}$ (at $z = 1.283$). Data have been visually rebinned to $S/N > 2$.

5. X-RAY OBSERVATIONS AND FUTURE PROSPECTS

Hard X-ray emission from blazars is important because it is directly connected to the central engine. The soft X-ray emission from blazars is thought to be due to synchrotron emission, while the hard X-ray emission is thought to be caused by up-scattering of soft photons either from the synchrotron emission (Mastichiadis & Kirk 2002), or from relatively cool structures like the accretion disk and the broad line region (Dermer & Schlickeiser 1993; Sikora 1994). While significant periodicities are common in the light curves of stellar mass black hole X-ray binary systems, they are surprisingly rare in AGN X-ray observations (however, see Juryšek et al. 2022). Only very recently have significant periodic signals started to be widely reported and studied systematically (Arcodia et al. 2021; Miniutti et al. 2019). In most cases, they originate in stellar-mass compact objects interacting with the AGN accretion disk (Franchini, Alessia et al. 2023). In the particular case of blazars, the X-ray light curves are usually chaotic and aperiodic. X-ray spectral-timing studies have revealed the existence of time-dependent flux density and spectral state patterns. Bhatta et al. (2018) explored the connections between blazar X-ray variability and other properties, such as spectral hardness and intrinsic X-ray flux in the *NuSTAR* band. All 13 sources in their sample displayed high-amplitude, rapid, aperiodic variability with a timescale of a few hours.

Since X-rays probe the region close to the central engine, the presence of a close-separation SMBHB could potentially imprint the high-energy emission. Simulations predict that close-separation accreting SMBHBs will have different X-ray spectra to those of single accreting SMBHBs (Tang et al. 2018; Krolik et al. 2019). Accreting SMBHBs may show a periodically modulated hard X-ray component whose period is of order the binary orbital period, although these predictions have been challenged (e.g., see Saade et al. 2023, 2024). There are no available high-quality X-ray data for PKS 2131–021, but short exposures during an *XMM-Newton* slew indicate a fairly high X-ray flux ($\sim 2 \times 10^{-12} \text{ erg s}^{-1} \text{ cm}^{-2}$) in the 2–12 keV range. We analyzed all available *Swift*/*XRT* observations. The stacked spectrum shown in Fig. 9 reaches a total net exposure time of 20.7 ks, characterized by a featureless power-law ($\Gamma = 1.78 \pm 0.15$) with a moderate intrinsic hydrogen column density of $N_{\text{H}} = 3.4^{+2.7}_{-2.4} \times 10^{21} \text{ cm}^{-2}$ at the rest-frame of $z = 1.283$. We estimate the 0.3–10 keV unabsorbed flux in the observed frame as $(1.86 \pm 0.15) \times 10^{-12} \text{ erg s}^{-1} \text{ cm}^{-2}$. In the near future, long-term monitoring with large-field-of-view instruments such as

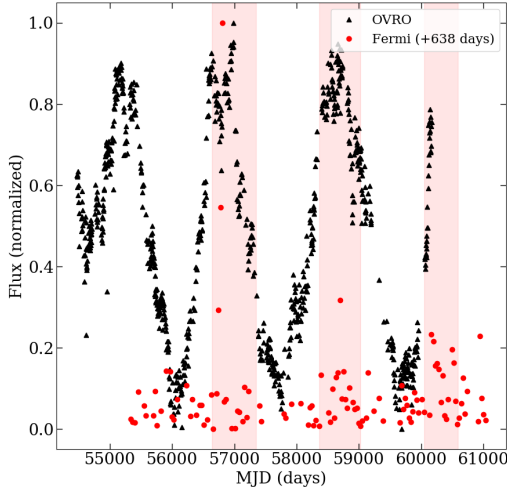


Figure 10. Normalized OVRO and Fermi light curves. The red shaded areas indicate the extent of the increased γ -ray activity. The γ -ray data have been shifted in time by 638 days to align the peaks in the radio and γ -ray observations (see text).

eRosita and *Swift* will be practical and promising, given the relatively high redshift of PKS 2131–021.

6. THE γ -RAY EMISSION

We used the Fermi light curve repository¹ (Abdollahi et al. 2023) to extract the 30-day binned γ -ray light curve in the 0.1–100 GeV band. The light curve was generated with the spectral index as a free parameter. We used the test statistic (TS) to identify, by eye, periods with increased significance indicating the presence of increased flux. We then identified the highest flux point in γ -rays which we match with the brightest radio flares by shifting the γ -ray data in time. We assumed the commonly accepted scenario in which the γ -rays come from a region upstream from the radio emission region (e.g., Liodakis et al. 2018).

Although γ -rays show sharper flares compared to the broad radio peaks, it is clear that the enhanced γ -ray activity periods, when shifted, align very well with the radio flares (Fig. 10). Depending on the radio peak, we can achieve a good alignment between radio and γ -rays with time-lags ranging between 454 and 819 days. If we shift the γ -rays forward by 638 days to match the radio-optical phase lag we obtain the comparison shown in Fig. 10, which appears to us a reasonable match, given the uncertainties. This is consistent with the monotonic

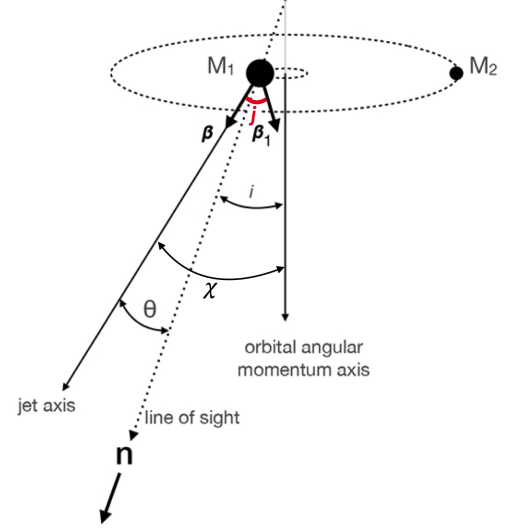


Figure 11. The KO model. In Paper 1 it was assumed that the angle between the jet axis, β , and the orbital angular velocity, β_1 , is $j \sim \pi/2$, leading to equation (8) in Paper 1. In this figure j is indicated in red.

phase trend shown in Fig. 6(d), which includes the time-lag found between radio and the WISE observations of 470 days (see Section 4.2). The fact that the radio– γ -ray time-lags are consistent with what we find for the infrared and optical observations suggests inverse-Compton scattering for the γ -ray production mechanism (e.g., Liodakis et al. 2019).

7. KINETIC ORBITAL MODEL

In this section we consider the implications of the new observations for the KO model, and explore the physical properties of PKS 2131–021 within the context of this model.

A schematic of the KO model is shown in Fig. 11. The model consists of a black hole binary. Expressing the masses of the binary components in units of $10^8 M_\odot$, the primary mass is $M_1 = 10^8 M_{18} M_\odot$, and the secondary mass is $M_2 = 10^8 M_{28} M_\odot$. Both masses orbit the center of mass with period in the rest frame of the binary $P = 761.8$ d, and angular momentum that makes an angle i with the line-of-sight unit vector \mathbf{n} . We assume that the motion has been circularized by frictional drag (Begelman et al. 1980), but elliptical orbits also work. We assume that the jet is launched along the spin axis of M_1 with fixed velocity $c\beta$ relative to the black hole. We know from the VLBI observations discussed in Appendix A that the line of sight is inclined at a small angle, θ , to the jet axis. The relationship between the orbital velocity of M_1 and β_1 is $\beta_1 = 0.036 M_{28} / (M_{18} + M_{28})^{2/3}$. Here we have set $c = 1$, and we do so for the rest of this section.

¹ <https://fermi.gsfc.nasa.gov/ssc/data/access/lat/LightCurveRepository/>

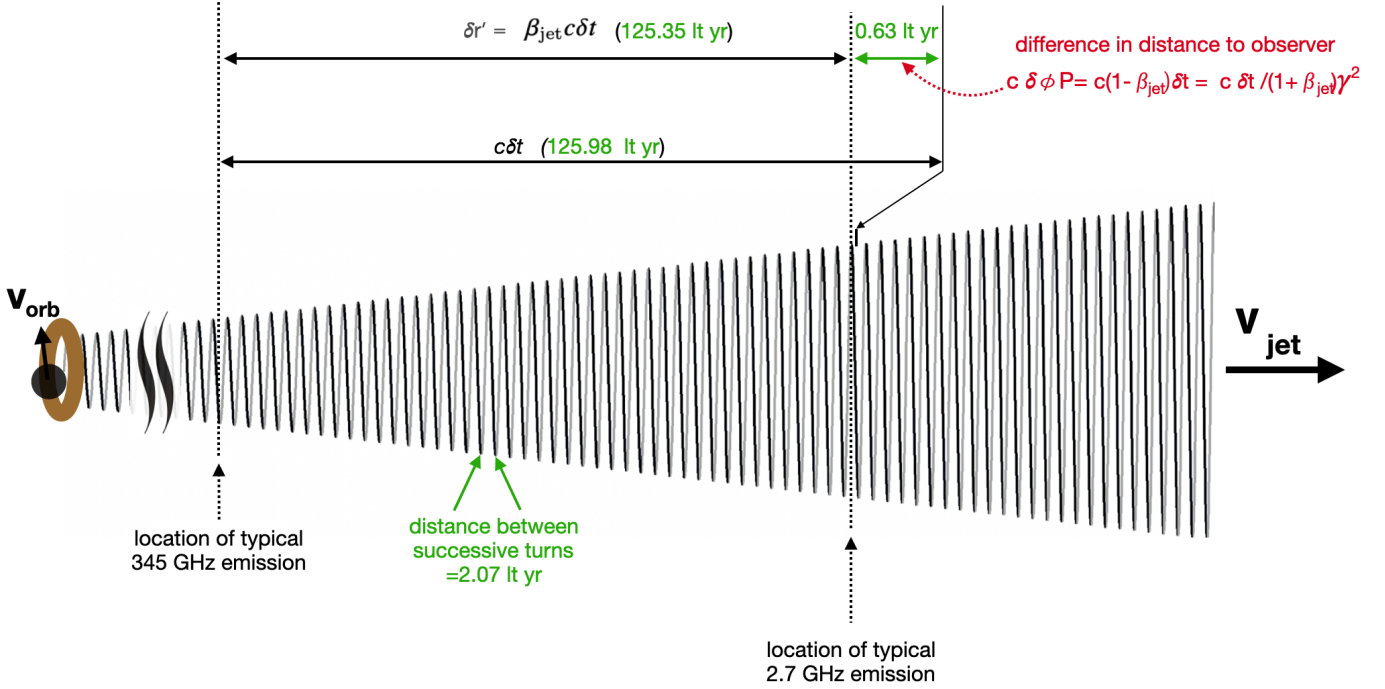


Figure 12. Schematic diagram (not to scale) showing the relationship between the typical locations of the emission at 345 GHz and 2.7 GHz on the KO model, for the case $\beta_1 = 0.020$, $\beta = 0.995$, and $\gamma \sim 10$. The numbers in green script correspond to this case. This schematic illustrates the special case where the orbital plane and the jet axis are orthogonal.

The orbital motion changes the velocity of the emitting material in the jet relative to the observer, and hence the Doppler factor and beaming. In the case of PKS 2131–021 the Doppler factor of the jet is high, so that the orbital motion can have a significant effect on the Doppler factor.

Suppose that we have a source at rest emitting isotropically and observed distantly with a flux density S' . The observed flux density will be given by $S = \mathcal{D}^{2-\alpha} S'$ (Scheuer & Readhead 1979), where $\alpha = d \ln S / d \ln \nu$ is the spectral index, and \mathcal{D} is the Doppler factor.

In this paper, as in Paper 1, in order to maximize the amplitude of the sinusoidal wave, we assume that the angle between the normal to the orbital plane and the line of sight, i , is ~ 0 .

7.1. Consistency of the observed light curves with the Kinetic Orbital Model

In Appendix A, we show, based on MOJAVE VLBI measurements, that the Doppler factor of the core component in PKS 2131–021 is $D = 14$, which, using the angle between the jet axis and the line of sight of $\theta = 3.8^\circ$ (Homan et al. 2021), yields a Lorentz factor $\gamma = 10$ (see Appendix A). We can perform a simple consistency check with the KO model using the phase shifts we have determined. This also provides some useful constraints

on the scales of the region producing the sinusoid in PKS 2131–021.

We assume that the emission of observed frequency ν comes from jet radius $r'(\nu)$ in the SMBHB rest frame. Taking into account light travel-time effects (see Fig. 12), the difference in $r'(\nu)$ between two phases observed simultaneously (assuming a head-on jet and $\beta \sim 1$) is

$$\delta r'(\nu) = \beta(1 + \beta)\gamma^2 c P_0 \delta \phi \sim 2\gamma^2 c P_0 \delta \phi, \quad (2)$$

where P_0 is the binary period in the rest frame of the host galaxy. Thus the difference in the distances of the emission sites at two frequencies, ν_1 and ν_2 , is

$$r(\nu_2) - r(\nu_1) = -0.25\gamma^2 c P_0 \log_{10}(\nu_2/\nu_1), \quad (3)$$

which implies that the frequency of the corresponding peaks in the sinusoidal variations as a function of radius satisfies

$$\nu = \nu_0 \exp[-r'/(0.069\gamma^2 \text{ pc})]. \quad (4)$$

Note that we cannot determine ν_0 with existing data because we only have phase differences. However, the fact that we determined this linear relation over a factor of 128 in ν implies that we are seeing at least 5 e -folding distances, so we can put a lower limit on r'

$$r' > 5 \times 0.069\gamma^2 \text{ pc} \sim 0.345\gamma^2 \text{ pc}, \quad (5)$$

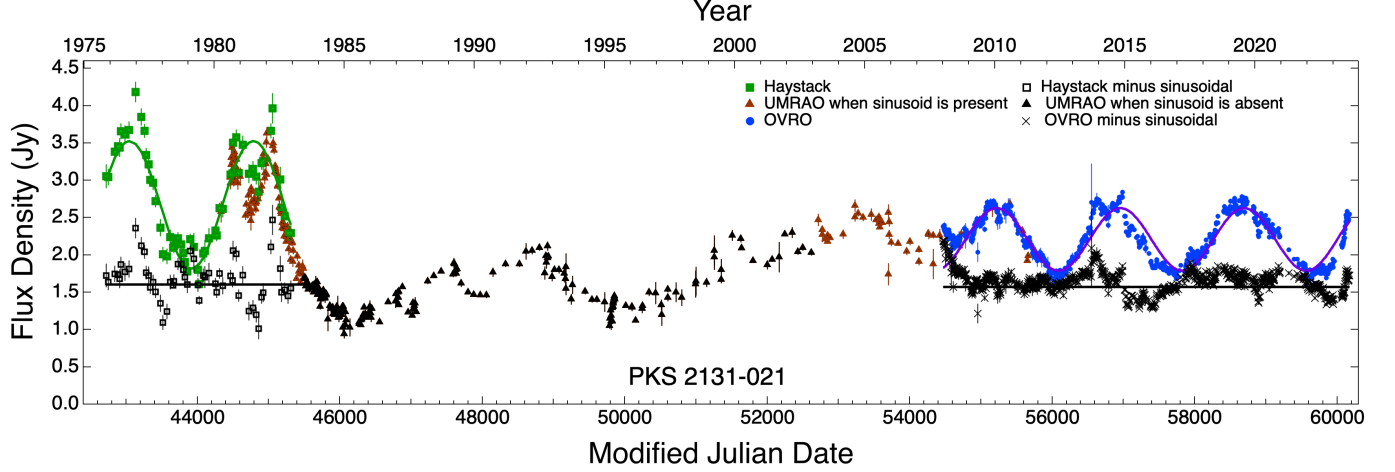


Figure 13. Sinusoidally-varying and non-sinusoidally-varying components in PKS 2131–021. Green squares: Haystack 15.5 GHz observations (O’Dea et al. 1986), together with the least-squares sine-wave fit (green line) to the data from Fig. 6(a). Black and brown triangles: UMRAO data (Aller et al. 1985, 2017). Blue circles: OVRO 15 GHz data, together with the best OVRO least squares sine wave fit (purple line) from Fig. 1(a), the parameters of which are given in Table 1. The black horizontal lines show the average level of the non-sinusoidally-varying component corresponding to a fractional variation of 0.72 in the sinusoidally varying components (see text). The black open square (cross) points show the Haystack (OVRO) residual non-sinusoidally-varying flux density after subtraction of the corresponding sine wave assuming this fractional variation of 0.72. Thus the black data points across the whole span of time show the light curve of PKS 2131–021 as it would appear without the sinusoidally varying component.

so that, based on the value of $\gamma = 10$,

$$r' \gtrsim 34.6 \text{ pc, i.e., } \sim 113 \text{ ly.} \quad (6)$$

This also gives a lower limit on the projected scale,

$$r'_{\text{proj}} = \theta r' > 0.345 \gamma^2 \theta \text{ pc} \quad (7)$$

i.e.,

$$r'_{\text{proj}} \gtrsim 2.3 \text{ pc, i.e. } \sim 7.5 \text{ ly,} \quad (8)$$

based on the values of $\theta = 3.8^\circ$ derived by Homan et al. (2021) and $\gamma = 10$.

In the light curve of PKS 2131–021 shown in Fig. 13, it can be seen that during the period when the sinusoidal signal was absent, from 1984 to 2003, the flux density varied between 1.0 Jy and 2.2 Jy. The horizontal black lines show the likely mean levels of the non-sinusoidal signal during the epochs when the sinusoidal signal was present. Any mean levels significantly different from these would lead to unlikely steps in the flux density level at the transition. We use these mean levels to determine the fractional change, $\delta S/S$, in flux density of the sinusoidal signal to be 0.72. The black points show the sinusoidal-signal-subtracted residual light curves. The smooth continuation of the light curves across the whole period (black points) is a result of the careful balancing we have done of the fractional change in flux density due to the sine wave and the mean level of the non-sinusoidal component, and shows that this balancing has been done correctly.

This fitting was done by eye, and it was done independently for the transitions at the end of the green sine wave and the beginning of the blue sine wave shown in Fig. 13. The mean levels without the sine waves, shown by the black horizontal lines differ by 2%, even though these fits were determined at transitions that are separated by 24 y. We also find that the mean level during the period when the sinusoidal variation was absent, marked by the black triangles, differs by only 7% from the mean of the residuals during the two periods when the sinusoidal variations were present. The good agreement between these mean levels lends credence to our hypothesis that there are underlying emission components that are not varying sinusoidally, shown by the black symbols in Fig. 13, and that the sinusoidal variations are seen as *an addition* to this underlying component.

We have not attempted here to subtract the sinusoidal signal during the period from 2003 to 2008, when it appears to have been switching on, because the amplitude was clearly changing. Note that the fractional variation in flux density of 0.72 is consistent with a value of $\beta_1 = 0.020$, and $\beta = 0.995$, i.e. $\gamma = 10$. For convenience we will adopt the value $\beta_1 = 0.020$.

As an instructive exercise and guide, we consider the KO model of in the rest frame of the SMBHB, in the case where the orbital plane and the jet axis are orthogonal. In this case the locus of the jet is a helix on the surface of a cone, as shown in Fig. 12, and the opening angle of the

cone is $2\beta_1/\beta$. From Equation 2 we see that with these parameters $\delta r'$ between the regions emitting at 2.7 GHz and 345 GHz is 125.35 ly, and the distance along the jet axis between successive turns of the helix is 2.07 ly. Thus there are ~ 60 turns of the helix between these two surfaces. At first sight it may seem strange that the phase difference between these two emission regions separated by over 60 cycles is so small, but this is simply a result of the fact that the jet is advancing at nearly the speed of light ($0.995c$), so that for any distance light travels along the jet axis, the jet falls behind by only $1/200$ of that distance, and thus, in ~ 60 rotations the jet falls behind by only 0.3 of a cycle. The surface from which the emission emerges at a given frequency is at a fixed distance from the SMBH, but the jet is moving through this stationary surface at speed v_{jet} . This is indistinguishable from the situation considered by Rees (1967). Our conclusion for this section is that the data are consistent with the KO model.

An important question is “At what level does one expect to see harmonics of the fundamental frequency?”. This is beyond the scope of the present paper, and will be discussed in a future paper. For the present, we refer the reader to Appendix B.

An interesting physical issue is why the dominant frequency emitted along the jet should depend exponentially on r' . The requirement of a well-defined spectral peak at each r' (as well as compactness and flat spectrum of the emitting region) suggests a transition from optically thick to thin radiation due to synchrotron self-absorption. It is hard to accomplish this if the jet properties are insensitive to radius, since the transition will not be abrupt enough, leading to phase mixing (e.g., resulting in strong 2.7 GHz radiation from a large range of radii) which will damp out the amplitude of the sinusoid. The most likely jet property to vary downstream is the magnetic field B in the jet and, in order to get the high frequency radiation to lead the low frequency in phase, we need the magnetic field to decrease exponentially along the jet.

This type of model offers an interesting working hypothesis. For example, one could imagine that some event (e.g., a recollimation shock or onset of Kelvin–Helmholtz instability) stirs up turbulence and turbulent resistivity, allowing the current flowing down the jet to leak out sideways. If this happens exponentially with r' , it will lead to an exponential decrease in B and a corresponding exponential decrease in ν with r' . This is an interesting physical problem in its own right, since it is usually assumed that the current has to leak out of the jet somewhere in order to close the circuit—this would

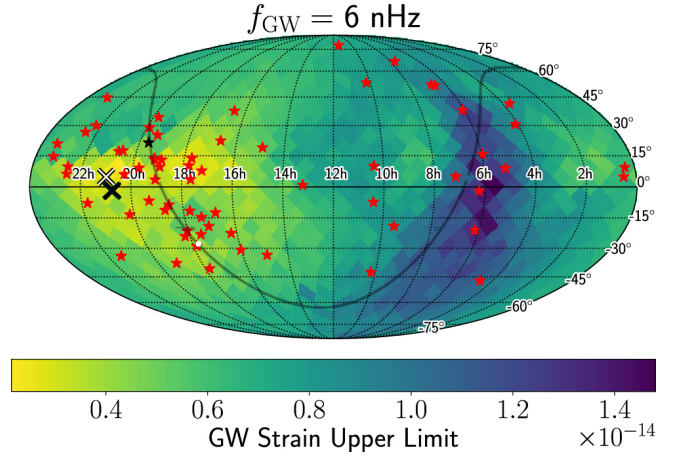


Figure 14. Mollweide projection of the sky in right ascension and declination coordinates, showing the position of PKS 2131–021 (black cross) plotted on the NANOGrav strain upper limits (Agazie et al. 2023b). The gray curve shows the Galactic Plane. The white dot marks the location of the Galactic center. The white cross marks the position of the highest NANOGrav sensitivity. The red asterisks mark the positions of the millisecond pulsars used in the Agazie et al. (2023b) analysis, from which this figure is adapted. The black asterisk marks the position of 4C 21.53, the first millisecond pulsar.

suggest that the leakage could occur very close to the central engine.

8. WHAT FRACTION OF BLAZARS ARE SMBHB CANDIDATES?

The recent discovery of a stochastic background of gravitational waves (GW) with periods of months to years (Agazie et al. 2023a; EPTA Collaboration et al. 2023) using millisecond pulsars as GW probes has promoted an intense search for the GW electromagnetic counterparts (e.g., Agazie et al. 2023b), which makes clear the importance of SMBHB searches such as the one we are engaged in with the OVRO 40 m Telescope. Millisecond pulsars (Readhead & Hewish 1974; Backer et al. 1982)² enable searches for gravitational waves with periods of months to years using pulsar timing arrays such as the European pulsar timing array (EPTA, Antoniadis et al. 2023), the North American Nanohertz Observatory for Gravitational Waves (NANOGrav, Agazie et al. 2023a,c,b), and the Parkes pulsar timing array (PPTA, Zic et al. 2023). As it happens, PKS 2131–021

² There were two crucial steps in the discovery of millisecond pulsars: (i) the discovery of interplanetary scintillation, at Galactic latitude -0.3° , in 4C 21.53 by Readhead & Hewish (1974) (see Readhead (2024)), which first drew attention to the singular nature of this object; and (ii) the discovery of millisecond pulses from 4C 21.53W by Backer et al. (1982).

is almost optimally located for study with the EPTA, NANOGrav, and the PPTA. In Fig. 14, the black and white crosses mark PKS 2131–021 and the location of greatest NANOGrav sensitivity, respectively (Agazie et al. 2023b).

It is clearly important to determine the fraction of blazars that are SMBHB candidates. We are in the process of carrying out a detailed study applying the above GLS analysis to all of the AGN in the 40 m monitoring sample. Since this study is in progress we give here only a brief outline of our findings thus far. We have completed the local significance analysis on about half of the objects in the sample, and we find that about 15% of these pass the 3σ local significance threshold. We have yet to carry out the global significance analysis on these objects. In the case of PKS 2131–021 the ratio of the local p -value to the global p -value is >40 . If we assume that the same applies to the other objects in the sample then we project that at most 20 of the objects in our sample will pass the 3σ global significance threshold. We have thus far found four AGN that pass the 3σ global significance threshold. Thus the projected fraction of AGN in our sample that are strong SMBHB candidates is at least 1 in 500, and could be 1 in 100.

However, it should be borne in mind that the test we are applying is selecting SMBHB candidates in which the sinusoidal variation is both strong and persists over most of the 16 year period of observations, from 2008 to 2023, inclusive. We have seen in PKS 2131–021 that the sinusoidal variation was absent for 19 of the past 48 years. In addition the sinusoidal variations have to be strong enough, compared to the random variations in the source, to yield a 3σ global significance. It appears very likely that there will be AGN that are SMBHBs in which there are sinusoidal signals that do not pass this threshold. For all of these reasons, in our view, the fraction of SMBHBs among jetted-AGN is likely to be ~ 1 in 100, or higher.

Such estimates from EM surveys can be compared to the observed value of the amplitude of the GW background, under the assumption that its origin is an ensemble of SMBHBs (e.g., Holgado et al. 2018; Inayoshi et al. 2018; Nguyen et al. 2020; Sesana et al. 2018). Based on an assumed quasar mass function and SMBHB candidates from the Catalina Real-Time Transient Survey, Casey-Clyde et al. (2024) estimated an upper limit of 25% on the fraction of quasars hosting an SMBHB. Holgado et al. (2018) presented an upper limit on the fraction of blazars that host an SMBHB with a period less than 5 yr assuming certain blazar population properties. Comparing this to an older upper limit on the GW amplitude at a frequency $f = 1$ yr

of $A_{\text{yr}} < 1.45 \times 10^{-15}$ at the 95% credible level (Arzoumanian et al. 2018) from the 11yr of NANOGrav dataset, they estimated a binary fraction of $\lesssim 0.1\%$. However, the updated GW amplitude values based on the NANOGrav 15yr dataset of $A_{\text{yr}} = 2.4^{+0.7}_{-0.6} \times 10^{-15}$ at the 90% level (Agazie et al. 2023a) implies a revised binary fraction to $\lesssim 0.5\%$. These estimates are roughly consistent with our estimate above.

It is interesting to note that JWST is finding a large number of dual AGN at high redshifts, some of which are separated by a few or several hundred parsecs (Perna et al. 2023; Marshall et al. 2023; Übler et al. 2023; Maiolino et al. 2023). The fraction of these dual AGN seems to be fairly high (20–30%), while the majority of AGN hosts have close companions or show post-merging signatures. While the fate of black holes in interacting galaxies at large (several-kiloparsec) separations is not yet clear (Di Matteo et al. 2023), black holes with separations of less than 1 kpc are expected to become black hole binaries on sinking times of a few to several hundred million years, especially given the high central stellar densities of these early galaxies, which increase the drag force on BHs. A fraction of such binary BHs with appropriate jet emission and orientation should be detectable as blazars, with periodic signals similar to those seen in PKS 2131–021 at $z = 1.283$. It is difficult to compare the fraction of blazars that are SMBHB candidates and the fraction of candidate BH mergers from recent JWST observations with theoretical models and simulations of BH merging, due to poor statistics and large uncertainties in both observations and simulations. However, these are all areas of active and rapid development, and a quantitative assessment might be possible in the near future.

9. CONCLUSION AND FUTURE WORK

The most important results of this paper are

1. The demonstration of continuing coherent sinusoidal variations in the flux density of PKS 2131–021 for a further 2 years.
2. An increase in the significance of the periodicity in PKS 2131–021 by a factor of 3.
3. The discovery that coherent strong sinusoidal variations in the flux density of PKS 2131–021 extend from below 2.7 GHz to optical wavelengths.
4. The discovery that the phases of the sinusoidal variations show a monotonically increasing lag with increasing observing wavelength.
5. The discovery that the short-term random fluctuations at optical wavelengths are an order of mag-

nitude or more greater than those at radio wavelengths, when compared with the amplitudes of the sinusoidal signals in these two wavebands.

6. The data are consistent with the KO model, in which the sinusoidal variation is caused by aberration due to the orbital motion of a jet-producing SMBH in an SMBHB.
7. Given the critical importance of the identification of the origin of the stochastic background of gravitational waves detected by PTAs, only carefully-vetted strong SMBHB candidates, of proven high statistical significance, should be used in PTA targeted searches.
8. The periodicity at radio wavelengths has remained persistent and stable across several epochs. The newly discovered periodicity in optical and possibly in γ -rays again shows the robustness of this discovery. We thus predict that this periodicity will persist with additional radio through γ -ray monitoring of this source.

It is clear that the periodicity we see in PKS 2131–021 is telling us something fundamental about this object. The possible causes of this periodicity that should be considered are (i) orbital motion of an SMBHB; (ii) precessional motion of the accretion disk; and (iii) a magneto-hydrodynamic (MHD) instability. We believe that (iii) can be ruled out by the fact that the sinusoidal variations disappeared for 19 years and then re-appeared with the same period and in phase with the original variations (see Paper 1). This is evidence of a “clock” continuously ticking during the 19-year gap in the sinusoidal variations. Of the remaining options (i) and (ii), neither can be ruled out, but it is clear that orbiting motion in an SMBHB is a distinct possibility. For this reason we believe that pulsar timing arrays should carry out coherent searches for gravitational waves from PKS 2131–021 and other strong well-vetted OVRO SMBHB candidates.

The Atacama Cosmology Telescope (ACT) (Li et al. 2023), and the South Pole Telescope (SPT) (Guns et al. 2021) have accumulated many years of data on tens of hundreds of blazars, which provide invaluable information on SMBHB candidates, and may well reveal new SMBHB candidates as these data are mined. With large-scale sky surveys, such as with the ZTF, the Vera Rubin Observatory, and the Simons Observatory (Ade et al. 2019), hundreds of thousands of blazars can be monitored for long periods. We now have several other strong SMBHB candidates in the OVRO monitoring sample, and, if the KO model is correct, there must be several SMBHB candidates that are difficult to detect

because of the dependence of the fractional variation in flux density on the angle of inclination of the orbital plane to the line of sight. Thus we estimate that the fraction of radio blazars that are SMBHB candidates is at least 1 in 100, which raises the clear possibility of detecting thousands of SMBHB candidates with well-determined periods.

ACKNOWLEDGEMENTS

We thank the California Institute of Technology and the Max Planck Institute for Radio Astronomy for supporting the OVRO 40 m program under extremely difficult circumstances over the last 10 years in the absence of agency funding. Without this private support these observations could not have been made. We also thank all the volunteers who have enabled this work to be carried out. Prior to 2016, the OVRO program was supported by NASA grants NNG06GG1G, NNX08AW31G, NNX11A043G, and NNX13AQ89G from 2006 to 2016 and NSF grants AST-0808050 and AST-1109911 from 2008 to 2014. S.K. & K.T. acknowledge support from the European Research Council (ERC) under the European Unions Horizon 2020 research and innovation programme under grant agreement No. 771282. I.L. and S.K. were funded by the European Union ERC-2022-STG - BOOTES - 101076343. Views and opinions expressed are however those of the author(s) only and do not necessarily reflect those of the European Union or the European Research Council Executive Agency. Neither the European Union nor the granting authority can be held responsible for them. W.M. acknowledges support from ANID project Basal FB210003. A.S. and R.B. acknowledge support by a grant from the Simons Foundation (00001470, RB, AS). R.R. acknowledges support from ANID Basal FB210003 and ANID-FONDECYT grant 1181620. C.O. acknowledges support from the Natural Sciences and Engineering Research Council (NSERC) of Canada. T.H. acknowledges support from the Academy of Finland projects 317383, 320085, 322535, and 345899. The NANOGrav collaboration receives support from National Science Foundation (NSF) Physics Frontiers Center award numbers 1430284 and 2020265. Part of this research was carried out at the Jet Propulsion Laboratory, California Institute of Technology, under a contract with the National Aeronautics and Space Administration. This paper makes use of the following ALMA data: ADS/JAO.ALMA#2011.0.00001.CAL. ALMA is a partnership of ESO (representing its member states), NSF (USA) and NINS (Japan), together with NRC (Canada), NSTC and ASIAA (Taiwan), and KASI (Republic of Korea), in cooperation with the Republic of

Chile. The Joint ALMA Observatory is operated by ESO, AUI/NRAO and NAOJ. The National Radio Astronomy Observatory is a facility of the National Science Foundation operated under cooperative agreement

by Associated Universities, Inc. This research has made use of the NASA/IPAC Extragalactic Database (NED), which is funded by the National Aeronautics and Space Administration and operated by the California Institute of Technology.

APPENDIX

A. KO MODEL PARAMETERS FOR THE SINUSOIDALLY VARYING CORE COMPONENT

Homan et al. (2021) were specifically interested in the PKS 2131-021 component brightness temperatures and they fitted all of the core regions in a consistent fashion, taking particular care not to mix components between epochs. The details of their approach are given in the methods section of their paper. They found a median $T_{b, \text{observed}} = 5.8 \times 10^{11} \text{K}$ over 24 epochs from 1995 to 2013. They also found an estimated intrinsic median brightness temperature for their sample of $T_{b, \text{intrinsic}} = 4.1 \times 10^{10} \text{K}$, which gives an estimated Doppler factor of $D = T_{b, \text{observed}}/T_{b, \text{intrinsic}} = 14$. Thus, using the value $\theta = 3.8^\circ$ determined by Homan et al. (2021), for this paper we adopt the value $\beta = 0.995$, corresponding to $\gamma = 10$ and $D = 14$. The amplitude of the 15 GHz OVRO light curve, assuming a fixed period $P = 1739.2$ days for the sinusoidal component, is 0.42 Jy. In order not to detect it, we need to suppress the amplitude of the first harmonic to below $0.1 \times$ the amplitude of the fundamental. Hence the amplitude of the first harmonic should be less than 42 mJy. A sinusoidal first harmonic of amplitude 42 mJy is shown in Fig. 16. To achieve this suppression of the amplitude of the first harmonic, we need a value of $\beta_1 \ll 1$, so we adopt a value $\beta_1 = 0.020$.

Note that from the MOJAVE results (Homan et al. 2021), which find an apparent speed of the fastest moving components of $19.9c \pm 2.6c$, we might expect to use a value of $\gamma \sim 20$. However, the structure that is making the sinusoidal variations is inside the core component. We have no guarantee that the γ value of the components within the core is the same as that of those outside of the core. On the KO model, a γ of 20 would make the radiation emission regions 4 times further away from the SMBH than a γ of 10, and we would like to try to keep this distance as small as allowed by the observations. The smallest value of γ that gives the observed fractional variation is $\gamma = 10$, so we adopt this value.

We now determine the equipartition angular size and the equipartition brightness temperature following Scott & Readhead (1977) and Readhead (1994), and using the updated expressions for the Λ CDM cosmology given by Readhead et al. (2021, Appendix B). In the course of this work we realized that there is a typographical error in the expression for $F(\alpha)$ given in Scott & Readhead (1977). The correct expression, using the α definition $S \propto \nu^{-\alpha}$ of Scott & Readhead (1977), is $F(\alpha) = 1.6C(\alpha)[(\nu_{\text{low}}^{1/2-\alpha} - \nu_{\text{high}}^{1/2-\alpha})/((2\alpha - 1)f_1(\alpha))]^{1/17} f_3(\alpha)^{-7/17}$, where ν_{low} and ν_{high} are the lower and upper cutoffs in the spectrum. The typographical error in Scott & Readhead (1977) is that the exponent $(-7/17)$ that applies to $f_3(\alpha)$ was omitted. Values of $C(\alpha)$ are tabulated by Scott & Readhead (1977), and the expression for $f_3(\alpha)$ is given by equation 15c of Scheuer & Williams (1968), and plotted by Readhead et al. (2021, Appendix B), but note the change in the sign of α between these two papers. We have recalculated the expressions for the equipartition angular size, ψ_{eq} , and equipartition brightness temperature, T_{eq} , to higher accuracy than given in Readhead et al. (2021), and in so doing discovered an error of $2^{1/17} = 1.042$. The corrected/revised expressions are given below.

In the Λ CDM cosmology the equipartition angular size becomes:

$$\psi_{\text{eq}} = 1.74 r^{-\frac{1}{17}} S^{\frac{8}{17}} \nu^{-\frac{35+2\alpha}{34}} (1+z)^{\frac{15-2\alpha}{34}} F(\alpha), \quad (\text{A1})$$

where r is the comoving coordinate distance in gigaparsec, S is the flux density in jansky at the peak of the spectrum, ν is the frequency at the peak in the spectrum in MHz, and $F(\alpha)$ is given in Scott & Readhead (1977), noting that they use the convention $S \propto \nu^{-\alpha}$. Hence we find $\psi_{\text{eq}} = 0.65$ mas for the core of PKS 2131-021.

The equipartition brightness temperature is given by

$$T_{\text{eq}} = 5.84 \times 10^{11} \left[\frac{r}{(1+z)} \right]^{2/17} F(\alpha)^{-2} (1+z)^{(2\alpha-13)/17} S^{1/17} (10^3 \nu)^{(1+2\alpha)/17} \text{K}. \quad (\text{A2})$$

and hence we find $T_{\text{eq}} = 1.98 \times 10^{10} \text{K}$. Note that this is a factor 2 lower than the value for $T_{b, \text{intrinsic}}$ adopted above. However the brightness temperatures that Homan et al. (2021) calculate are the Gaussian brightness temperatures,

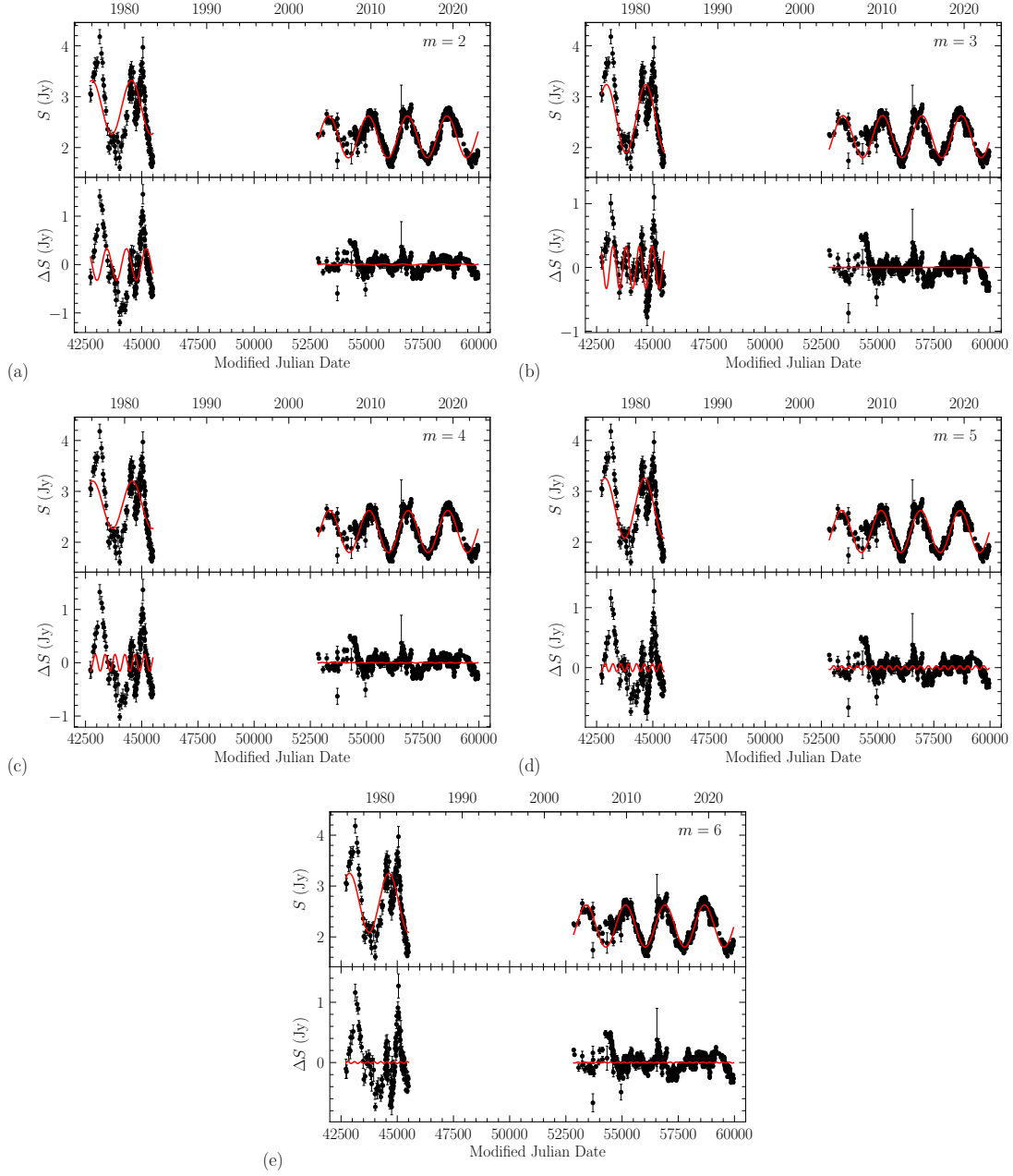


Figure 15. Absence of higher harmonics in the 15 GHz light curve of PKS 2131–021. In (a)–(e) the upper panels show the original light curves and the sine wave fits for $m = 2$ –6, and the lower panels show the residual light curves after subtraction of the sine wave fits.

which must be reduced by a factor 1.8 to compare with those of [Readhead \(1994\)](#). This reduces the $T_{b,\text{intrinsic}}$ to 2.3×10^{10} K, which implies a ratio of particle to magnetic field energy densities of ~ 4 ([Readhead 1994](#)).

B. THE ABSENCE OF HIGHER HARMONICS

To check if any higher harmonic frequencies are present in the data, we fitted the following models to the radio light curve:

$$S(t) = A_1 \sin(\phi - \phi_0) + A_3 \sin((\phi - \phi_0)m) + S_1$$

for $\text{MJD} < 45500$, and

$$S(t) = A_2 \sin(\phi - \phi_0) + A_4 \sin((\phi - \phi_0)m) + S_2$$

for $\text{MJD} > 52850$, where $m = 2, 3, 4, 5, 6$ and $\phi = 2\pi(t - t_0)/P$, $t_0 = 51000$. The best-fit parameters were found by maximizing the likelihood function defined as:

$$\ln \mathcal{L} = -\frac{1}{2} \sum_i^{t < 45500} \left(\frac{(S_i - S(t_i))^2}{\sigma_i^2 + \sigma_1^2} + \ln(\sigma_i^2 + \sigma_1^2) \right) - \frac{1}{2} \sum_i^{t > 52800} \left(\frac{(S_i - S(t_i))^2}{\sigma_i^2 + \sigma_2^2} + \ln(\sigma_i^2 + \sigma_2^2) \right). \quad (\text{B3})$$

In Fig. 15 we show the plots of the harmonics fits and in Table 4 we show the results of the fits. We used the Bayesian information criterion (BIC) to check if models with harmonic frequencies provide a better fit than a simple sine wave model. The BIC is calculated as follows $\text{BIC} = -2 \ln \mathcal{L}_{\text{max}} + k \ln n$, where \mathcal{L}_{max} is the maximum value of the likelihood function, k is the number of parameters estimated by the model, and n is the number of data points. For $m = 2$, $m = 4$, and $m = 6$, $\delta\text{BIC} \gtrsim 0$, so the simpler model is preferred. The model with $m = 3$ results in BIC that is smaller by $\delta\text{BIC} = -49.6$ than in the simpler model, which formally provides positive evidence that the former model is preferred. However, the improvement comes mostly from Haystack data and the OVRO data do not provide any evidence for the $m = 3$ harmonic. It is safe to assume that this is due to over-fitting of the Haystack data. For $m = 5$, the BIC improvement is smaller ($\delta\text{BIC} = -15.8$), which is likely due to over-fitting of the OVRO data.

We found the best-fit amplitude of the first harmonic ($m = 2$) to be 0.012 ± 0.006 Jy (the 95% upper limit was 0.022 Jy). The model with the first harmonic had $\text{BIC} = -2664.7$, and it was smaller by $\delta(\text{BIC}) = -0.4$ than the BIC of the model without the first harmonic, showing that the former model is slightly, but not significantly, preferred.

In order to test for a possible first harmonic, we carried out the following exercise. We added an artificial sinusoidal signal with a period of $P/2$, and an amplitude of 0.012 Jy to the data. We then fitted sine-wave models (with and without the first harmonic) to the synthetic data. The best-fit amplitude of the first harmonic was 0.025 ± 0.006 Jy, and the BIC of the model with the first harmonic was $\text{BIC} = -2661.7$. The BIC for the model without harmonics was -2665.0 , so $\delta(\text{BIC}) = +3.3$. When we added an artificial sinusoidal signal with an amplitude of 0.025 Jy, the best-fit amplitude of the first harmonic was 0.036 ± 0.006 Jy, and $\delta(\text{BIC}) = -31.3$. In conclusion, we find that an amplitude of the first harmonic of 0.025 Jy is just consistent (at the 2σ level) with the data assuming random variations. Given that the variations are clearly not random, as can be seen by the black points in Fig. 16, which show long-term correlated fluctuations, the level of consistency is considerably better than this. So a first harmonic of amplitude 42 mJy cannot be ruled out by the data.

C. SINE-WAVE FITS TO THE OPTICAL DATA

We fitted the following sine-wave model to the optical data:

$$m(t) = A \sin(\phi - \phi_0) + m_0, \quad (\text{C4})$$

where $\phi = 2\pi(t - t_0)/P$, and $t_0 = 59000$. The best-fit parameters were found by maximizing the log-likelihood function defined as

$$\ln \mathcal{L} = -\frac{1}{2} \sum_{g,r,i} \sum_{j=1}^{N_{\text{obs}}} \left(\frac{(m_j - m_j^{\text{model}})^2}{\sigma_j^2 + \sigma_0^2} + \ln(\sigma_j^2 + \sigma_0^2) \right). \quad (\text{C5})$$

Table 4. Fit results for the Haystack and OVRO 15 GHz data assuming $t_0 = 51000$.

	no harm.	$m = 2$	$m = 3$	$m = 4$	$m = 5$	$m = 6$
P (d)	1755.8 ± 4.9	1776.5 ± 4.4	1738.1 ± 1.2	1767.1 ± 5.0	1755.7 ± 3.5	1755.8 ± 4.8
ϕ_0 (rad)	0.728 ± 0.064	0.457 ± 0.056	0.964 ± 0.016	0.578 ± 0.064	0.733 ± 0.046	0.731 ± 0.063
A_1 (Jy)	0.563 ± 0.059	0.528 ± 0.058	0.666 ± 0.032	0.478 ± 0.062	0.566 ± 0.054	0.562 ± 0.063
A_3 (Jy)	...	0.307 ± 0.074	0.319 ± 0.030	< 0.239	< 0.144	< 0.100
S_1 (Jy)	2.679 ± 0.042	2.783 ± 0.045	2.574 ± 0.023	2.736 ± 0.043	2.685 ± 0.037	2.675 ± 0.042
σ_1 (Jy)	0.390 ± 0.033	0.441 ± 0.030	0.239 ± 0.018	0.430 ± 0.030	0.387 ± 0.030	0.390 ± 0.033
A_2 (Jy)	0.414 ± 0.007	0.411 ± 0.006	0.414 ± 0.007	0.414 ± 0.006	0.415 ± 0.006	0.414 ± 0.007
A_4 (Jy)	...	< 0.022	< 0.010	< 0.017	0.032 ± 0.006	< 0.019
S_2 (Jy)	2.212 ± 0.005	2.211 ± 0.004	2.214 ± 0.005	2.212 ± 0.004	2.212 ± 0.004	2.212 ± 0.005
σ_2 (Jy)	0.126 ± 0.004	0.122 ± 0.003	0.133 ± 0.004	0.124 ± 0.004	0.124 ± 0.003	0.126 ± 0.004
$\ln \mathcal{L}_{\text{max}}$	1359.8	1366.9	1391.5	1361.1	1374.6	1360.5
BIC	-2664.3	-2664.7	-2713.9	-2653.1	-2680.1	-2651.9
δBIC	0.0	-0.4	-49.6	+11.2	-15.8	+12.4

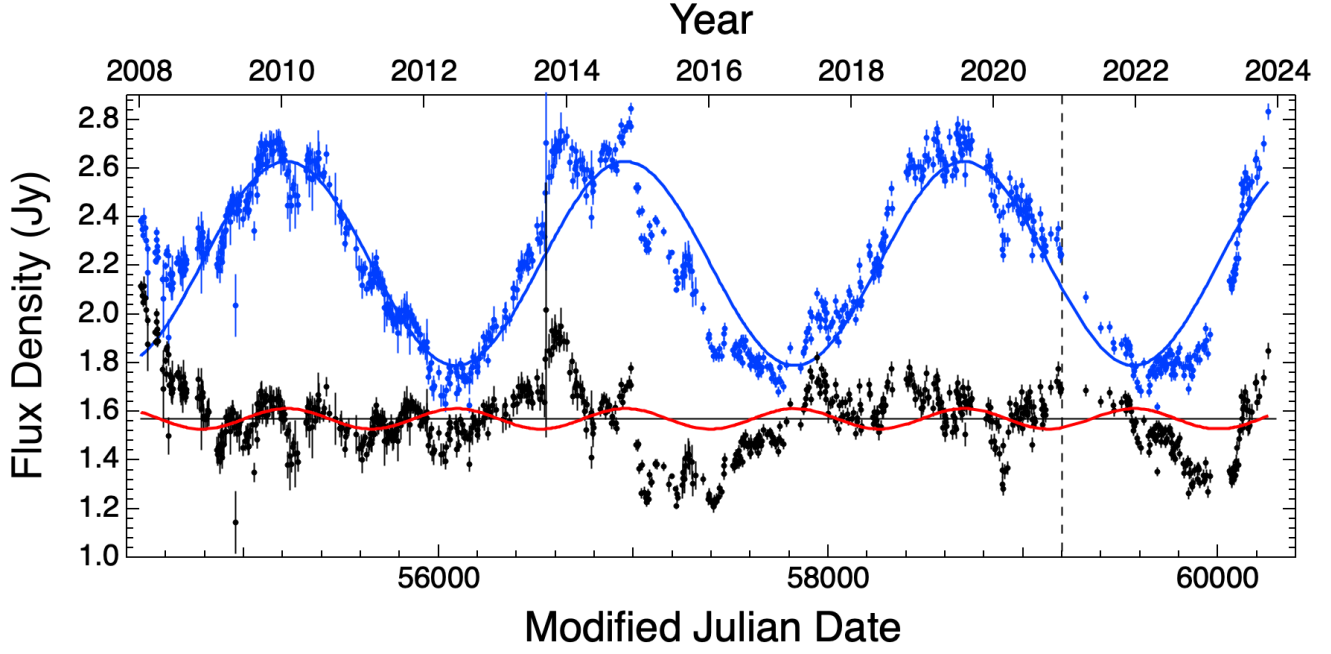


Figure 16. A first harmonic of amplitude 0.042 Jy is shown by the red curve. Sinusoidal first harmonic fluctuations of this amplitude cannot be ruled out by our data (see Appendix A), because of the non-Gaussian nature of the noise, which clearly has long-term correlated fluctuations at this level. Other symbols and curves are the same as those in Fig. 13.

First, we assumed that the period and phase are identical for all filters, but the amplitudes, mean magnitudes, and σ_0 may depend on the passband (model 1). Subsequently, we relaxed this assumption and allowed the sine phases to depend on the filter (model 2). Results of the fits are reported in Table 5.

Table 5. Results of the sine-wave fits to the optical data

Parameter	Value	
P (d)	1764 ± 36	1762 ± 36
ϕ_0 (rad)	4.372 ± 0.056	...
ϕ_0 (r)	...	4.353 ± 0.080
ϕ_0 (g)	...	4.349 ± 0.084
ϕ_0 (i)	...	4.456 ± 0.113
m_0 (r)	17.454 ± 0.021	17.453 ± 0.021
A (r)	0.358 ± 0.032	0.358 ± 0.032
σ_0 (r)	0.363 ± 0.015	0.363 ± 0.015
m_0 (g)	18.030 ± 0.022	18.030 ± 0.022
A (g)	0.366 ± 0.033	0.366 ± 0.034
σ_0 (g)	0.383 ± 0.016	0.383 ± 0.016
m_0 (i)	17.146 ± 0.035	17.155 ± 0.037
A (i)	0.379 ± 0.055	0.388 ± 0.058
σ_0 (i)	0.376 ± 0.023	0.376 ± 0.023
$\chi^2/\text{d.o.f.}$	785.4/780	786.7/778

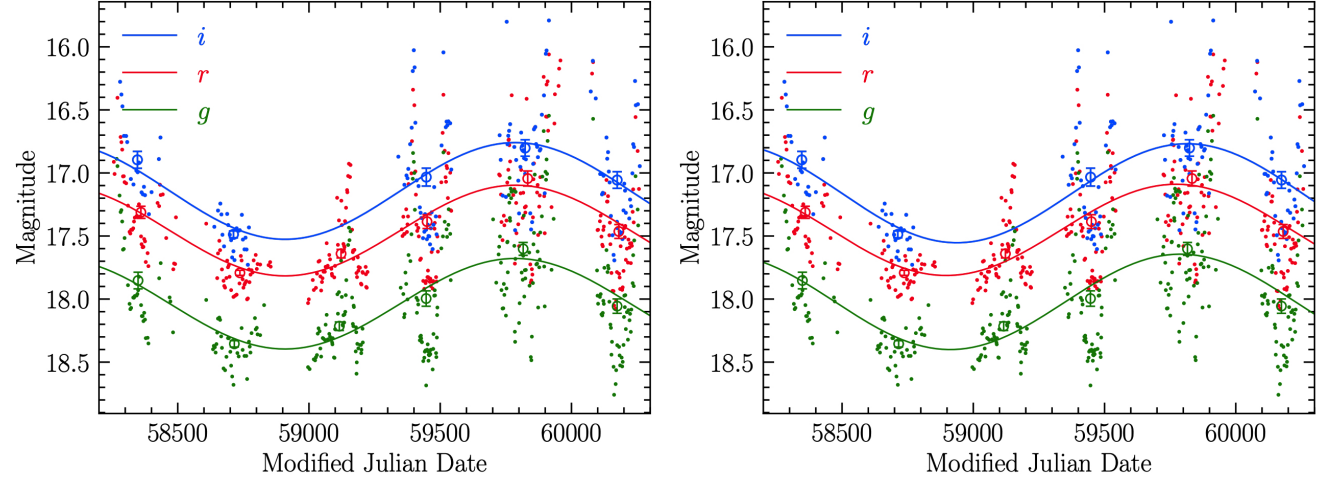


Figure 17. Best-fit sine-wave models to the optical data, assuming that the periods and phases are identical in all filters (left panel) or allowing the phases to depend on the passband (right panel).

REFERENCES

- Abdollahi, S., Ajello, M., Baldini, L., et al. 2023, *ApJS*, 265, 31, doi: [10.3847/1538-4365/acbb6a](https://doi.org/10.3847/1538-4365/acbb6a)
- Ackermann, M., Ajello, M., Albert, A., et al. 2015, *ApJL*, 813, L41, doi: [10.1088/2041-8205/813/2/L41](https://doi.org/10.1088/2041-8205/813/2/L41)
- Ade, P., Aguirre, J., Ahmed, Z., et al. 2019, *JCAP*, 2019, 056, doi: [10.1088/1475-7516/2019/02/056](https://doi.org/10.1088/1475-7516/2019/02/056)
- Agazie, G., Anumalapudi, A., Archibald, A. M., et al. 2023a, *ApJL*, 951, L8, doi: [10.3847/2041-8213/acdac6](https://doi.org/10.3847/2041-8213/acdac6)
- . 2023b, *ApJL*, 951, L50, doi: [10.3847/2041-8213/ace18a](https://doi.org/10.3847/2041-8213/ace18a)
- . 2023c, *ApJL*, 952, L37, doi: [10.3847/2041-8213/ace18b](https://doi.org/10.3847/2041-8213/ace18b)
- Aller, H. D., Aller, M. F., Latimer, G. E., & Hodge, P. E. 1985, *ApJS*, 59, 513, doi: [10.1086/191083](https://doi.org/10.1086/191083)
- Aller, M. F., Aller, H. D., & Hughes, P. A. 2017, *Galaxies*, 5, 75, doi: [10.3390/galaxies5040075](https://doi.org/10.3390/galaxies5040075)
- Aller, M. F., Aller, H. D., Hughes, P. A., & Latimer, G. E. 1999, *ApJ*, 512, 601, doi: [10.1086/306799](https://doi.org/10.1086/306799)
- Antoniadis, J., Arumugam, P., Arumugam, S., et al. 2023, *arXiv e-prints*, arXiv:2306.16226, doi: [10.48550/arXiv.2306.16226](https://doi.org/10.48550/arXiv.2306.16226)
- Arcodia, R., Merloni, A., Nandra, K., et al. 2021, *Nature*, 592, 704, doi: [10.1038/s41586-021-03394-6](https://doi.org/10.1038/s41586-021-03394-6)
- Arzoumanian, Z., Baker, P. T., Brazier, A., et al. 2018, *ApJ*, 859, 47, doi: [10.3847/1538-4357/aabd3b](https://doi.org/10.3847/1538-4357/aabd3b)
- Backer, D. C., Kulkarni, S. R., Heiles, C., Davis, M. M., & Goss, W. M. 1982, *Nature*, 300, 615, doi: [10.1038/300615a0](https://doi.org/10.1038/300615a0)
- Begelman, M. C., Blandford, R. D., & Rees, M. J. 1980, *Nature*, 287, 307, doi: [10.1038/287307a0](https://doi.org/10.1038/287307a0)
- Bhatta, G., Mohorian, M., & Bilinsky, I. 2018, *A&A*, 619, A93, doi: [10.1051/0004-6361/201833628](https://doi.org/10.1051/0004-6361/201833628)
- Blandford, R., Meier, D., & Readhead, A. 2019, *ARA&A*, 57, 467, doi: [10.1146/annurev-astro-081817-051948](https://doi.org/10.1146/annurev-astro-081817-051948)
- Casey-Clyde, J. A., Mingarelli, C. M. F., Greene, J. E., et al. 2024, *arXiv e-prints*, arXiv:2405.19406, doi: [10.48550/arXiv.2405.19406](https://doi.org/10.48550/arXiv.2405.19406)
- Dermer, C. D., & Schlickeiser, R. 1993, *ApJ*, 416, 458, doi: [10.1086/173251](https://doi.org/10.1086/173251)
- Dey, L., Valtonen, M. J., Gopakumar, A., et al. 2021, *MNRAS*, 503, 4400, doi: [10.1093/mnras/stab730](https://doi.org/10.1093/mnras/stab730)
- Di Matteo, T., Ni, Y., Chen, N., et al. 2023, *MNRAS*, 525, 1479, doi: [10.1093/mnras/stad2198](https://doi.org/10.1093/mnras/stad2198)
- D’Orazio, D. J., & Charisi, M. 2023, *arXiv e-prints*, arXiv:2310.16896, doi: [10.48550/arXiv.2310.16896](https://doi.org/10.48550/arXiv.2310.16896)
- EPTA Collaboration, InPTA Collaboration, Antoniadis, J., et al. 2023, *A&A*, 678, A50, doi: [10.1051/0004-6361/202346844](https://doi.org/10.1051/0004-6361/202346844)
- Franchini, Alessia, Bonetti, Matteo, Lupi, Alessandro, et al. 2023, *A&A*, 675, A100, doi: [10.1051/0004-6361/202346565](https://doi.org/10.1051/0004-6361/202346565)
- Gabuzda, D. C., Pushkarev, A. B., & Cawthorne, T. V. 2000, *MNRAS*, 319, 1109, doi: [10.1046/j.1365-8711.2000.03932.x](https://doi.org/10.1046/j.1365-8711.2000.03932.x)
- Graham, M. J., Djorgovski, S. G., Stern, D., et al. 2015, *Nature*, 518, 74, doi: [10.1038/nature14143](https://doi.org/10.1038/nature14143)
- Graham, M. J., Kulkarni, S. R., Bellm, E. C., et al. 2019, *PASP*, 131, 078001, doi: [10.1088/1538-3873/ab006c](https://doi.org/10.1088/1538-3873/ab006c)
- Guns, S., Foster, A., Daley, C., et al. 2021, *ApJ*, 916, 98, doi: [10.3847/1538-4357/ac06a3](https://doi.org/10.3847/1538-4357/ac06a3)
- Holgado, A. M., Sesana, A., Sandrinelli, A., et al. 2018, *MNRAS*, 481, L74, doi: [10.1093/mnrasl/sly158](https://doi.org/10.1093/mnrasl/sly158)
- Homan, D., Hovatta, T., Kovalev, Y., et al. 2018, *Galaxies*, 6, 17, doi: [10.3390/galaxies6010017](https://doi.org/10.3390/galaxies6010017)
- Homan, D. C., & Lister, M. L. 2006, *AJ*, 131, 1262, doi: [10.1086/500256](https://doi.org/10.1086/500256)
- Homan, D. C., Lister, M. L., Aller, H. D., Aller, M. F., & Wardle, J. F. C. 2009, *ApJ*, 696, 328, doi: [10.1088/0004-637X/696/1/328](https://doi.org/10.1088/0004-637X/696/1/328)
- Homan, D. C., Cohen, M. H., Hovatta, T., et al. 2021, *ApJ*, 923, 67, doi: [10.3847/1538-4357/ac27af](https://doi.org/10.3847/1538-4357/ac27af)
- Hovatta, T., & Lindfors, E. 2019, *NewAR*, 87, 101541, doi: [10.1016/j.newar.2020.101541](https://doi.org/10.1016/j.newar.2020.101541)
- Hovatta, T., Lister, M. L., Aller, M. F., et al. 2012, *AJ*, 144, 105, doi: [10.1088/0004-6256/144/4/105](https://doi.org/10.1088/0004-6256/144/4/105)
- Hovatta, T., Aller, M. F., Aller, H. D., et al. 2014, *AJ*, 147, 143, doi: [10.1088/0004-6256/147/6/143](https://doi.org/10.1088/0004-6256/147/6/143)
- Inayoshi, K., Ichikawa, K., & Haiman, Z. 2018, *ApJL*, 863, L36, doi: [10.3847/2041-8213/aad8ad](https://doi.org/10.3847/2041-8213/aad8ad)
- Jones, T. W., & O’Dell, S. L. 1977, *ApJ*, 214, 522, doi: [10.1086/155278](https://doi.org/10.1086/155278)
- Juryšek, J., Sliusar, V., Moulin, D., & Walter, R. 2022, in *37th International Cosmic Ray Conference*, 643, doi: [10.22323/1.395.0643](https://doi.org/10.22323/1.395.0643)
- Komatsu, E., Dunkley, J., Nolte, M. R., et al. 2009, *ApJS*, 180, 330, doi: [10.1088/0067-0049/180/2/330](https://doi.org/10.1088/0067-0049/180/2/330)
- Krolik, J. H., Volonteri, M., Dubois, Y., & Devriendt, J. 2019, *ApJ*, 879, 110, doi: [10.3847/1538-4357/ab24c9](https://doi.org/10.3847/1538-4357/ab24c9)
- Li, Y., Biermann, E., Naess, S., et al. 2023, *ApJ*, 956, 36, doi: [10.3847/1538-4357/ace599](https://doi.org/10.3847/1538-4357/ace599)
- Liodakis, I., Romani, R. W., Filippenko, A. V., et al. 2018, *MNRAS*, 480, 5517, doi: [10.1093/mnras/sty2264](https://doi.org/10.1093/mnras/sty2264)
- Liodakis, I., Romani, R. W., Filippenko, A. V., Kocovski, D., & Zheng, W. 2019, *ApJ*, 880, 32, doi: [10.3847/1538-4357/ab26b7](https://doi.org/10.3847/1538-4357/ab26b7)
- Lomb, N. R. 1976, *Ap&SS*, 39, 447, doi: [10.1007/BF00648343](https://doi.org/10.1007/BF00648343)
- Maiolino, R., Scholtz, J., Curtis-Lake, E., et al. 2023, *arXiv e-prints*, arXiv:2308.01230, doi: [10.48550/arXiv.2308.01230](https://doi.org/10.48550/arXiv.2308.01230)

- Marshall, M. A., Perna, M., Willott, C. J., et al. 2023, *A&A*, 678, A191, doi: [10.1051/0004-6361/202346113](https://doi.org/10.1051/0004-6361/202346113)
- Masci, F. J., Laher, R. R., Rusholme, B., et al. 2019, *PASP*, 131, 018003, doi: [10.1088/1538-3873/aae8ac](https://doi.org/10.1088/1538-3873/aae8ac)
- Mastichiadis, A., & Kirk, J. G. 2002, *PASA*, 19, 138, doi: [10.1071/AS01108](https://doi.org/10.1071/AS01108)
- Max-Moerbeck, W., Richards, J. L., Hovatta, T., et al. 2014, *MNRAS*, 445, 437, doi: [10.1093/mnras/stu1707](https://doi.org/10.1093/mnras/stu1707)
- Miniutti, G., Saxton, R. D., Giustini, M., et al. 2019, *Nature*, 573, 381, doi: [10.1038/s41586-019-1556-x](https://doi.org/10.1038/s41586-019-1556-x)
- Nguyen, K., Bogdanović, T., Runnoe, J. C., et al. 2020, *ApJL*, 900, L42, doi: [10.3847/2041-8213/abb2ab](https://doi.org/10.3847/2041-8213/abb2ab)
- O'Dea, C. P., Dent, W. A., Kinzel, W. M., & Balonek, T. J. 1986, *AJ*, 92, 1262, doi: [10.1086/114260](https://doi.org/10.1086/114260)
- O'Neill, S., Kiehlmann, S., Readhead, A. C. S., et al. 2022, *ApJL*, 926, L35, doi: [10.3847/2041-8213/ac504b](https://doi.org/10.3847/2041-8213/ac504b)
- O'Sullivan, S. P., McClure-Griffiths, N. M., Feain, I. J., Gaensler, B. M., & Sault, R. J. 2013, *MNRAS*, 435, 311, doi: [10.1093/mnras/stt1298](https://doi.org/10.1093/mnras/stt1298)
- Perna, M., Arribas, S., Lamperti, I., et al. 2023, arXiv e-prints, arXiv:2310.03067, doi: [10.48550/arXiv.2310.03067](https://doi.org/10.48550/arXiv.2310.03067)
- Peterson, B. M., Wanders, I., Horne, K., et al. 1998, *PASP*, 110, 660, doi: [10.1086/316177](https://doi.org/10.1086/316177)
- Planck Collaboration, Aghanim, N., Akrami, Y., et al. 2020, *A&A*, 641, A6, doi: [10.1051/0004-6361/201833910](https://doi.org/10.1051/0004-6361/201833910)
- Pushkarev, A. B., Aller, H. D., Aller, M. F., et al. 2023, *MNRAS*, 520, 6053, doi: [10.1093/mnras/stad525](https://doi.org/10.1093/mnras/stad525)
- Readhead, A. C. S. 1980, in *Objects of High Redshift*, ed. G. O. Abell & P. J. E. Peebles, Vol. 92, 165–175
- Readhead, A. C. S. 1994, *ApJ*, 426, 51, doi: [10.1086/174038](https://doi.org/10.1086/174038)
- Readhead, A. C. S. 2024, arXiv e-prints, arXiv:2406.17164, <https://arxiv.org/abs/2406.17164>
- Readhead, A. C. S., Cohen, M. H., Pearson, T. J., & Wilkinson, P. N. 1978, *Nature*, 276, 768, doi: [10.1038/276768a0](https://doi.org/10.1038/276768a0)
- Readhead, A. C. S., & Hewish, A. 1974, *MmRAS*, 78, 1
- Readhead, A. C. S., Ravi, V., Liodakis, I., et al. 2021, *ApJ*, 907, 61, doi: [10.3847/1538-4357/abd08c](https://doi.org/10.3847/1538-4357/abd08c)
- Rees, M. J. 1967, *MNRAS*, 135, 345, doi: [10.1093/mnras/135.4.345](https://doi.org/10.1093/mnras/135.4.345)
- Richards, J. L., Max-Moerbeck, W., Pavlidou, V., et al. 2011, *ApJS*, 194, 29, doi: [10.1088/0067-0049/194/2/29](https://doi.org/10.1088/0067-0049/194/2/29)
- Rocha, G., Keskitalo, R., Partridge, B., et al. 2023, *A&A*, 669, A92, doi: [10.1051/0004-6361/202141995](https://doi.org/10.1051/0004-6361/202141995)
- Saade, L., Stern, D., Brightman, M., et al. 2023, in *American Astronomical Society Meeting Abstracts*, Vol. 55, American Astronomical Society Meeting Abstracts, 177.31
- Saade, M. L., Brightman, M., Stern, D., et al. 2024, *ApJ*, 966, 104, doi: [10.3847/1538-4357/ad372e](https://doi.org/10.3847/1538-4357/ad372e)
- Scargle, J. D. 1982, *ApJ*, 263, 835, doi: [10.1086/160554](https://doi.org/10.1086/160554)
- Scheuer, P. A. G., & Readhead, A. C. S. 1979, *Nature*, 277, 182, doi: [10.1038/277182a0](https://doi.org/10.1038/277182a0)
- Scheuer, P. A. G., & Williams, P. J. S. 1968, *ARA&A*, 6, 321, doi: [10.1146/annurev.aa.06.090168.001541](https://doi.org/10.1146/annurev.aa.06.090168.001541)
- Scott, M. A., & Readhead, A. C. S. 1977, *MNRAS*, 180, 539, doi: [10.1093/mnras/180.4.539](https://doi.org/10.1093/mnras/180.4.539)
- Sesana, A., Haiman, Z., Kocsis, B., & Kelley, L. Z. 2018, *ApJ*, 856, 42, doi: [10.3847/1538-4357/aaad0f](https://doi.org/10.3847/1538-4357/aaad0f)
- Sikora, M. 1994, *ApJS*, 90, 923, doi: [10.1086/191926](https://doi.org/10.1086/191926)
- Sillanpää, A., Haarala, S., Valtonen, M. J., Sundelius, B., & Byrd, G. G. 1988, *ApJ*, 325, 628, doi: [10.1086/166033](https://doi.org/10.1086/166033)
- Sobacchi, E., Sormani, M. C., & Stamerra, A. 2017, *MNRAS*, 465, 161, doi: [10.1093/mnras/stw2684](https://doi.org/10.1093/mnras/stw2684)
- Tang, Y., Haiman, Z., & MacFadyen, A. 2018, *MNRAS*, 476, 2249, doi: [10.1093/mnras/sty423](https://doi.org/10.1093/mnras/sty423)
- Übler, H., Maiolino, R., Pérez-González, P. G., et al. 2023, arXiv e-prints, arXiv:2312.03589, doi: [10.48550/arXiv.2312.03589](https://doi.org/10.48550/arXiv.2312.03589)
- . 2024, *MNRAS*, 531, 355, doi: [10.1093/mnras/stae943](https://doi.org/10.1093/mnras/stae943)
- Valtonen, M. J., Zola, S., Ciprini, S., et al. 2016, *ApJL*, 819, L37, doi: [10.3847/2041-8205/819/2/L37](https://doi.org/10.3847/2041-8205/819/2/L37)
- Vitrichchak, V. M., Gabuzda, D. C., Algaba, J. C., et al. 2008, *MNRAS*, 391, 124, doi: [10.1111/j.1365-2966.2008.13919.x](https://doi.org/10.1111/j.1365-2966.2008.13919.x)
- Volonteri, M., Haardt, F., & Madau, P. 2003, *ApJ*, 582, 559, doi: [10.1086/344675](https://doi.org/10.1086/344675)
- Xin, C., & Haiman, Z. 2021, *MNRAS*, 506, 2408, doi: [10.1093/mnras/stab1856](https://doi.org/10.1093/mnras/stab1856)
- Zic, A., Reardon, D. J., Kapur, A., et al. 2023, *PASA*, 40, e049, doi: [10.1017/pasa.2023.36](https://doi.org/10.1017/pasa.2023.36)